The Astrophysical Journal Letters, 999:L36 (16pp), 2026 March 10 https://doi.org/10.3847/2041-8213/ae4746

Dynamics of Planetary Rings under Thermal Forces

Wen-Han Zhou[1], Eiichiro Kokubo[2,3,4], Harrison Agrusa[5,6], Gregorio Ricerchi[5], Aurélien Crida[5],
David Vokrouhlický[7], Yun Zhang[8], and Ronald-Louis Ballouz[9]
[1] JSPS International Research Fellow, Department of Earth and Planetary Science, The University of Tokyo, Tokyo, Japan; wenhan.zhou@oca.eu
[2] Division of Science, National Astronomical Observatory of Japan, Mitaka, Tokyo, Japan
[3] Center for Computational Astrophysics, National Astronomical Observatory of Japan, Tokyo, Japan
[4] Department of Astronomy, University of Tokyo, Tokyo, Japan
[5] Université Côte d'Azur, Observatoire de la Côte d'Azur, CNRS, Laboratoire Lagrange, Nice, France
[6] Centre national d'études spatiales (CNES), Paris, France
[7] Astronomical Institute, Charles University, V Holešovičkách 2, CZ 18000, Prague 8, Czechia
[8] Department of Climate and Space Sciences and Engineering, University of Michigan, Ann Arbor, MI 48109, USA
[9] Johns Hopkins University Applied Physics Lab, Laurel, MD, USA

Received 2025 December 8; revised 2026 February 12; accepted 2026 February 17; published 2026 March 6

Abstract

Planetary rings provide natural laboratories for studying the fundamental processes that govern the evolution of planetary systems. However, several key features, such as the sharp inner edges of Saturn's rings, remain unresolved. In this Letter, we introduce and quantify the eclipse–Yarkovsky (EY) effect, a thermal torque arising from asymmetric thermal emission of particles during planetary eclipses, which is effective for particles larger than millimeters in size. We formulate this effect within a continuum framework appropriate for collisionally coupled planetary rings and derive the continuum evolution equation that includes the EY torque and viscous diffusion (Equation (26)), constraining its magnitude using ring particle spin distributions obtained from *N*-body simulations. We find that the EY effect systematically produces a positive angular momentum flux that could overcome the viscous torque, driving ring material outward and leading to long-term decretion. The total EY torque principally depends on the optical depth, in which we identify three dynamical regimes: dense, transitional, and tenuous, each exhibiting distinct evolutionary pathways. In the dense and transitional regimes, the EY torque can produce a sharp inner edge such as that of Saturn's A ring. In the tenuous regime, it can drive an entire ring outward while preserving shape. This outward transport may also facilitate satellite formation beyond the Roche limit. We also quantitatively show that planetary thermal radiation exerts an opposing torque, namely the planetary–Yarkovsky effect, whose importance depends on planetary emissivity and ring-particle albedo, and may lead to inward transport in Saturn's close-in rings.

Unified Astronomy Thesaurus concepts: Planetary rings (1254); Solar system (1528); Exoplanet rings (494); Planetary science (1255)

1. Introduction

All giant planets in the solar system host rings composed of small particles (typically $\leqslant$ a few meters), with Saturn's rings being the most massive and well studied. These systems serve as natural laboratories for exploring key dynamical processes—collisions, self-gravity, resonances, and angular momentum transport—that govern planetary system evolution (e.g., P. Goldreich & S. Tremaine 1978a, 1978b; L. Esposito 2014; J. Fuller 2014; M. S. Tiscareno & C. D. Murray 2018; Y. Kambara & E. Kokubo 2025; N. Torii et al. 2025). Over time, viscous spreading can drive material beyond the Roche limit to form moons, explaining the observed mass–distance distribution of planetary satellites (A. Crida & S. Charnoz 2012). Mars' moons Phobos and Deimos have similarly been proposed to originate from a past ring system (A. J. Hesselbrock & D. A. Minton 2017).

However, several puzzles remain in our understanding of ring evolution and structure. One long-standing issue is the presence of sharp edges in Saturn's major rings. While the outer edges can be explained by the balance between positive viscous torques and negative Lindblad torques from nearby moonlets, the sharp inner edges (e.g., of the A and B rings) are not well understood due to the lack of confining inner satellites that could supply the necessary resonant torques (e.g., A. Crida et al. 2025). One proposed mechanism is ballistic transport, in which high-speed impacts from micrometeoroids eject debris from ring particles (R. H. Durisen 1984; W.-H. Ip 1984; R. H. Durisen et al. 1989; J. N. Cuzzi & R. H. Durisen 1990). These ejecta follow ballistic trajectories and reaccrete elsewhere in the ring, effectively redistributing mass and angular momentum. Ballistic transport tends to move the mass and angular momentum of the inner edge outwards and is capable of maintaining sharp edges. This process cannot create sharp edges; it can only maintain an existing sharp edge. Another puzzle is related to a theoretical past Martian ring, which would have existed if Phobos and Deimos formed from a giant impact followed by accretion from a circumplanetary disk (S. F. Singer 1967; R. G. Strom et al. 1992; R. A. Craddock 2011; R. I. Citron et al. 2015; P. Rosenblatt et al. 2016; R. Canup & J. Salmon 2018). Dynamical models suggest that past Martian rings should persist for billions of years due to the long timescale of viscous spreading (A. J. Hesselbrock & D. A. Minton 2017; G. Madeira et al. 2023), but no ring is observed today. Together, these issues point to missing physics in current models of ring evolution.

In this Letter, we introduce a previously underappreciated thermal recoil effect, referred to here as the eclipse–Yarkovsky

(EY) effect, as a mechanism that may help resolve these puzzles. While this Letter mostly takes Saturn's ring systems as the example, the theory developed is sufficiently general that it is applicable to other planetary ring systems.

This Letter is organized as follows: Section 2 offers an overview and historical context of the EY effect. Section 3 derives the general form of the continuum equation, with the EY term given a particle size–frequency distribution (SFD). Section 4 calculates the EY term based on the distribution of particle rotation obtained from the *N*-body simulations, and Section 5 presents the long-term evolution by numerically solving the continuum equation incorporating the EY effect and discusses different regimes of the EY effect according to the optical depth. Finally we discuss the implications of the EY effect for the ring systems in the solar system in Section 6 and summarize our findings in Section 7.

2. The Eclipse–Yarkovsky Effect: an Overview and Historical Context

2.1. Radiation Forces in Celestial Mechanics: Historical Background

The concept of radiation pressure in modern physics arose from development of Maxwell's electromagnetic theory by a group of enthusiastic students and followers after his premature death in 1879, with Poynting playing a central role in clarifying its physical implications (see R. Loudon & C. Baxter 2012 for a concise overview). Although there existed earlier speculations about the role of sunlight pressure in the context of astronomical phenomena, these lacked both quantitative theoretical estimates and experimental confirmation. This changed in the early twentieth century, when P. Lebedew (1910) experimentally confirmed the existence of radiation pressure in agreement with Maxwell's theory.

Heliocentric orbital dynamics are directly influenced by such radiation-driven forces. While the direct sunlight pressure is conservative, other radiation-related nonconservative effects were also discovered and accurately described. Given today's perspective, the prime examples consist of (1) the Poynting–Robertson effect (S. P. Wyatt & F. L. Whipple 1950, based on its original formulation by J. H. Poynting 1904; H. P. Robertson 1937), and (2) the Yarkovsky effect, resurrected by E. J. Öpik (1951). J. A. Burns et al. (1979) published a masterful overview of the radiation processes and their role in planetary astronomy in the second half of the 20th century; additional information on the Yarkovsky effect is given by W. F. Bottke et al. (2006) and D. Vokrouhlický et al. (2015).

The essence of the Yarkovsky effect consists of the recoil due to the thermal radiation of the body. Because of thermal inertia, the emission over the surface is anisotropic: the hotter afternoon side experiences larger recoil than the cooler night side of the surface. The net effect integrated over the whole surface is generally tilted from the radial direction with a nonzero along-track projection. As a result, the effect leads to an accumulated change in semimajor axis, either positive or negative depending on the rotational state. This is the solar diurnal variant of the effect, conceptually pictured by E. J. Öpik (1951) and summarized by J. A. Burns et al. (1979, with more intermediate reference therein). In the next decades, it was realized that there exists also a solar seasonal[10] variant of the Yarkovsky effect (D. P. Rubincam 1987, 1988; V. J. Slabinski 1997), which is caused by the thermal lag over the heliocentric orbital motion (see Figure 1 of W. F. Bottke et al. 2006). The mathematical solution of the Yarkovsky effect for a spherical object was finally given by D. Vokrouhlický (1999).

The quantitative study of thermal recoil forces was catalyzed by the dynamics of Earth-heated satellites (e.g., D. P. Rubincam 1982, 1990; G. Afonso et al. 1989; P. Farinella et al. 1990; P. Farinella & D. Vokrouhlický 1996; V. J. Slabinski 1997) and later asteroid dynamics (e.g., G. Afonso et al. 1995; D. P. Rubincam 1995; P. Farinella et al. 1998). The widespread acceptance of the Yarkovsky effect by the community followed especially after the first direct detection of the heliocentric orbit drift of asteroid 6489 Golevka by S. R. Chesley et al. (2003). These studies demonstrated that even minute radiation-driven accelerations can cause significant orbital evolution over long timescales. Since then, Yarkovsky-induced transverse accelerations have been measured for hundreds of asteroids (e.g., X. Liu et al. 2023; M. Fenucci et al. 2024) and are now archived online. In the asteroid population, the Yarkovsky effect is a key mechanism driving long-term orbital evolution of meter- to kilometer-scale bodies. It produces systematic drift in the semimajor axis that creates near-Earth object populations from the main belt, shapes the age and structure of asteroid families, and enables constraints on asteroid bulk density and thermal properties when combined with astrometric observations (see review by W. F. Bottke et al. 2006; D. Vokrouhlický et al. 2015).

Planetocentric orbital dynamics under an external heating source, which describes a situation when sunlight heats a small satellite (or dust particle) orbiting a planet, stemmed again from the field of satellite geodesy. J. A. Burns et al. (1979) discuss the case of the solar radiation pressure for such a configuration, noting that the principal long-term perturbation concerns the planetocentric eccentricity and pericenter, which helps in understanding the structure of Jupiter's tiny dust rings (e.g., D. P. Hamilton & A. V. Krivov 1996) or rarefied regions in Saturn's system (e.g., M. M. Hedman et al. 2013). However, the role of planetary shadow is neglected in these early studies.

2.2. Eclipse-modulated Yarkovsky Forces

In a simple planetocentric configuration without eclipses, the solar-driven Yarkovsky force acting on a particle typically averages to zero over one planetocentric orbit: phases of positive and negative along-track acceleration cancel due to symmetry. This cancellation, however, is fundamentally broken when the particle experiences eclipses by the planet.

When a particle enters the planetary shadow, its surface cools and thermal emission is temporarily suppressed. Upon reemergence into sunlight, the surface reheats with a delay set by the particle's thermal inertia. The resulting asymmetry between cooling and heating phases produces a net thermal recoil force that does not vanish upon orbital averaging. Figure 1 shows a schematic of eclipses in a planetary ring. The magnitude and sign of this effect depend on the particle's spin state, thermal properties, and orbital geometry.

This eclipse-modulated thermal effect has appeared in the literature under various names. It was realized in the detailed analysis of the orbital decay of the LAGEOS spacecraft, where a variation correlated with periods when the spacecraft orbit crossed the Earth's shadow. D. P. Rubincam (1982) attributed the idea to Milton Schach, thus coining the term "Schach"

---

[10] In this work, we define "solar season" as the (thermal) variations driven by the planet's heliocentric orbit, while "planetary season" denotes the variations resulting from the rapid planetocentric orbital cycles of particles.

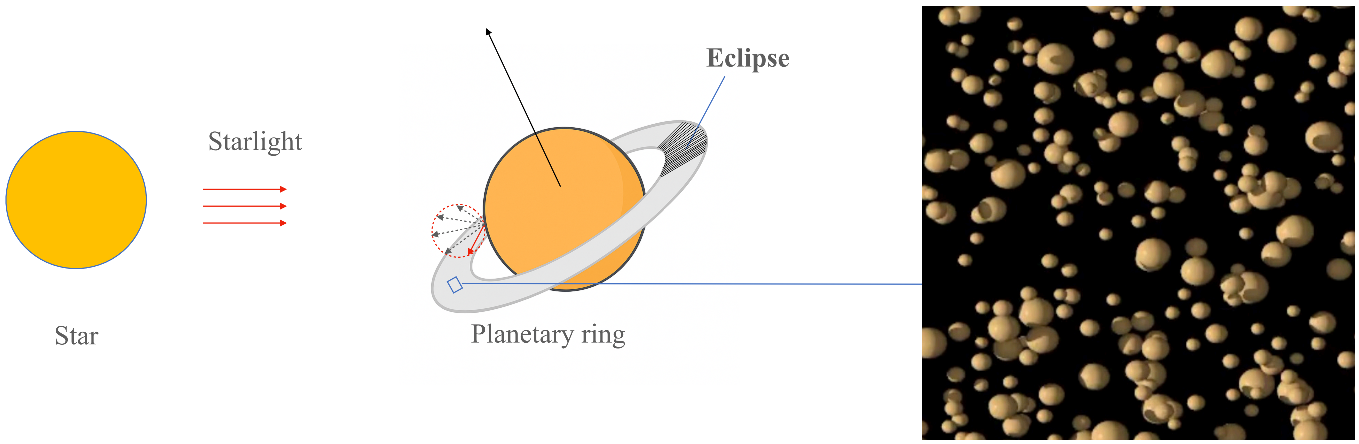

Figure 1. Schematic of the planetary ring with a shadow. The planet is surrounded by a ring tilted at an angle of ∼20°, mirroring the configuration of Mars or Saturn. The radiation from a surface element of the planet follows Lambert's emission law, denoted by the arrows within the red dashed circle. The thermal force arises from the thermal emission of particles. In particular, the eclipse leads to an asymmetric thermal emission of particles and therefore produces a net thermal torque after averaging the orbit, namely the eclipse–Yarkovsky effect. The right panel shows a simulated box with ring particles as an example.

(D. P. Rubincam 1982) or "Yarkovsky–Schach effect" (D. P. Rubincam 1990; P. Farinella & D. Vokrouhlický 1996; D. P. Rubincam 2006; D. Vokrouhlický et al. 2007), even though the latter did not present any published reference. Coincidentally, the very same concept was also discovered previously by Y. Boudon et al. (1979), who named the effect "photon thrust" or "thermal thrust," which was used by G. Afonso et al. (1989) and P. Farinella et al. (1990). In the context of binary asteroids (D. Vokrouhlický et al. 2005), it was called the "differential Yarkovsky" effect in some literature (P. Scheirich et al. 2015, 2021, 2024). Despite the diversity of terminology, these studies describe closely related manifestations of eclipse-modulated thermal recoil arising from the same underlying physical mechanism.

Analytical formulations of this effect for individual objects were developed by D. P. Rubincam (2006) and D. Vokrouhlický et al. (2007) and were discussed in the context of Saturn's rings. D. P. Rubincam (2014) further considers the effect introduced by the particle's thermal strain. While early works focused on the planetary seasonal component of this effect (e.g., Figure 1 of D. P. Rubincam 1982), more recent work by W.-H. Zhou et al. (2024) and W.-H. Zhou (2024) revisited this effect for both planetary seasonal and diurnal components of a binary asteroid system, explicitly tracking its dependence on the spin state and obliquity of asteroids. These studies showed that the diurnal component of this effect can move the object toward an orbit of synchronous rotation where the spin period equals the orbital period. On top of this, for misaligned objects, the diurnal component also has components that can induce an outward drift. W.-H. Zhou (2024) unified this eclipse-modulated effect with the planetary–Yarkovsky effect under the single designation of the "binary Yarkovsky" effect. Alongside the "binary YORP" effect (M. Ćuk & J. A. Burns 2005), this provides a comprehensive thermal framework for binary systems.[11]

The principal caveat of the work of D. P. Rubincam (2006) and D. Vokrouhlický et al. (2007) in Saturn's rings consisted in treating the ring particles individually as if they were isolated from the surrounding population. The role of coupling between the particles was only briefly touched on in Section 10 of D. P. Rubincam (2006) and Appendix F of D. Vokrouhlický et al. (2007), but no analysis of the varying optical depth across the ring was provided. Yet, the collective phenomena have long been recognized as crucial for understanding Saturn's ring system.

2.3. From Individual Particles to a Collisional Continuum

The primary objective of this Letter is to formulate this eclipse-modulated Yarkovsky effect within a continuum framework that would allow one to connect the potential importance of the thermal dynamical phenomena with the collective behavior of the planetary rings. The key physical insight is that the torque (i.e., net angular momentum flux) generated by the EY effect acting on individual particles is redistributed to neighboring particles through collisions, which conserve angular momentum. This is the essence that allows the ring annulus to respond collectively and therefore to be integrated into the continuum equation. In this setting, the relevant quantity is not the drift of an isolated object, but the redistribution of angular momentum across the ring. We therefore introduce the physically transparent term "eclipse–Yarkovsky effect" that is applicable to both single-body and ring-dynamical contexts and we emphasize the central physical role of eclipses in driving the thermal recoil. At the level of individual particles, this effect reduces to the classical Yarkovsky–Schach effect (or other names in the literature) in the context of binary asteroids or Earth satellites.

To get a preliminary insight into the importance of this effect, we estimate its timescale for individual particles of radius r orbiting at planetocentric distance R, defined as $R/\dot{R}$ (W.-H. Zhou et al. 2024):

$$t_{\mathrm{EY}} \simeq 1.1\ \mathrm{Gyr} \times \left(\frac{r_{\mathrm{p}}}{10^5\ \mathrm{km}}\right)\left(\frac{r}{0.1\ \mathrm{m}}\right)\left(\frac{R}{2r_{\mathrm{p}}}\right)^{1/2} \times \left(\frac{0.003}{f_{\mathrm{EY,norm}}}\right)\left(\frac{a_{\mathrm{h}}}{10\ \mathrm{au}}\right)^2, \quad (1)$$

where r_{p} is the planet's radius, a_{h} is heliocentric distance, and $f_{\mathrm{EY,norm}}$ is the EY coefficient anchored at $R = 2r_{\mathrm{p}}$, which

---

[11] Unlike the binary Yarkovsky effect, binary YORP requires long-term synchronous rotation and is equally likely to generate positive or negative torques. Consequently, it does not produce a systematic effect at the level of planetary rings, where particle orientations and shapes are expected to be randomly distributed.

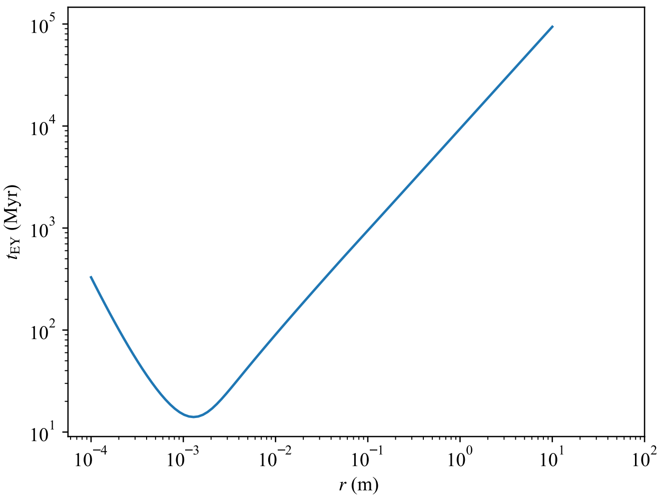

Figure 2. The timescale of the EY effect for individual particles as a function of their size for Saturn's system. The planetocentric distance is set to be 2 planetary radii and the EY coefficient $f_{\rm EY} = 0.002$.

measures the efficiency of the EY effect. The planet obliquity $\varepsilon_{\rm p}$ is assumed to be zero in Equation (1). This scaling is valid only for particles larger than the thermal penetration depth $r_0 \sim 1$ mm, while coverage over a smaller size would require the analytical solution of the EY effect (Equations (10), (11), and (12)). Figure 2 shows the timescales for different particle sizes in Saturn's ring system. We adopted $f_{\rm EY,norm} = 0.003$, as will be demonstrated in Section 4. On the other hand, the viscous evolution timescale is

$$t_{\rm visc} \sim \frac{R^2}{\nu} \simeq 32\ {\rm Gyr} \times \left(\frac{R}{10^5\ {\rm km}}\right)^2 \left(\frac{\nu}{10^{-2}\ {\rm m^2\ s^{-1}}}\right)^{-1}, \tag{2}$$

where ν is the viscosity. The viscosity depends on the surface density and material properties, and ranges from 0.003 to 0.03 $\rm m^2\ s^{-1}$ for Saturn's A and B rings and is $\sim 10^{-4}$ for Saturn's C ring (see, e.g., R. Tajeddine et al. 2017; M. S. Tiscareno & B. E. Harris 2018; A. Crida et al. 2025). It can be seen that the timescale for the EY effect in the Saturnian system could be shorter than the viscous evolution timescale for the size range from millimeters to meters. Due to the stronger solar radiation at Mars, the EY effect could be one hundred times stronger than for the Saturn system.

Accurate evaluation of the EY torque requires the particles' spin-state distribution (spin rate and obliquity). Using a realistic distribution from numerical simulations, we show that the population-averaged EY torque is positive, driving particles outward (Section 4). While the possibility of a positive eclipse-modulated torque has been noted previously (D. P. Rubincam 2006; D. Vokrouhlický et al. 2007), the present work offers a systematic investigation of how the EY effect affects the long-term evolution of planetary rings, by quantifying the strengths of this effect and integrating it into the continuum equations that govern ring surface density.

3. Theory

3.1. General Formula

In this section, we derive the one-dimensional evolution equation for planetary rings, incorporating the angular momentum flux introduced by the eclipse–Yarkovsky effect. The magnitude and direction of this flux will be discussed in the next section.

Consider a planetary ring characterized by a surface density profile $\Sigma(R, t)$ and a radial velocity $v_R(R, t)$ driven by dynamical mechanisms. We examine an annular segment of the ring with inner radius R and radial width ΔR, which therefore contains a mass $2\pi R \Delta R \Sigma$. By mass conservation, the rate of change of mass within this annulus equals the net difference between the mass inflow through the inner boundary and the outflow through the outer boundary:

$$\begin{aligned}\frac{\partial}{\partial t}(2\pi R \Delta R \Sigma) &= 2\pi R \times \Sigma(R, t) \times v_R(R, t)\\ &-2\pi(R + \Delta R) \times \Sigma(R + \Delta R, t) \times v_R(R + \Delta R, t).\end{aligned} \tag{3}$$

Taking the limit $\Delta R \to 0$, we obtain the continuity equation:

$$R\frac{\partial \Sigma}{\partial t} + \frac{\partial}{\partial R}(R \Sigma v_R) = 0. \tag{4}$$

Similarly, conservation of angular momentum yields

$$\begin{aligned}\frac{\partial}{\partial t}(2\pi R \Delta R \times \Sigma R^2 \Omega) &= 2\pi R \times \Sigma(R, t) R^2 \Omega(R) v_R(R, t)\\ &- 2\pi(R + \Delta R) \times \Sigma(R + \Delta R, t)(R + \Delta R)^2\\ &\times \Omega(R + \Delta R) v_R(R + \Delta R, t) + \Delta J,\end{aligned} \tag{5}$$

where $\Omega(R)$ is the planetocentric orbital frequency of the particle, and ΔJ denotes the net angular momentum exchange due to additional mechanisms. A dominant contribution to ΔJ arises from interparticle collisions driven by Keplerian shear (i.e., the radial differential motion between neighboring ring particles in a corotating Keplerian frame). This angular momentum exchange can be approximated as the difference in viscous torque across the annulus:

$$\begin{aligned}\Delta J = &-3\pi R^2 \nu(R, t) \Sigma(R, t) \Omega(R)\\ &+ 3\pi(R + \Delta R)^2 \nu(R + \Delta R, t) \Sigma\\ &\times (R + \Delta R, t) \Omega(R + \Delta R).\end{aligned} \tag{6}$$

Taking the limit $\Delta R \to 0$, the angular momentum conservation equation becomes

$$\frac{\partial}{\partial t}(\Sigma R^2 \Omega) + \frac{1}{R}\frac{\partial}{\partial R}(\Sigma R^3 \Omega v_R) = -\frac{3}{2R}\frac{\partial}{\partial R}(\nu \Sigma R^2 \Omega). \tag{7}$$

Combining Equations (4) and (7), we recover the classical evolution equation for the surface density of a viscously spreading ring:

$$\frac{\partial \Sigma}{\partial t} = \frac{3}{R}\frac{\partial}{\partial R}\left(\sqrt{R}\frac{\partial}{\partial R}(\nu \Sigma \sqrt{R})\right). \tag{8}$$

The EY effect introduces an additional torque term $T_{\rm EY}$ on the right-hand side of Equation (5). We begin by computing the magnitude of this torque.

The EY force, defined as the thermal force component along the planetocentric orbital velocity vector averaged over a planetocentric orbit, acting on a single ring particle at an arbitrary layer with the normal optical depth τ' (note that τ' is different from τ, which accounts for the full thickness) is given by W.-H. Zhou et al. (2024):

$$F_{\rm EY} = \frac{(1 - A_{\rm v})\, \Phi_{\rm s} \pi r^2}{c} e^{-\tau'/\sin\psi} f_{\rm EY}, \tag{9}$$

where Φ_s is the stellar flux (e.g., for the Sun, $\Phi_s \approx 1365\ \mathrm{W\,m^{-2}}$ at 1 au), A_v is the particle's albedo in the visible band, r is the particle radius, c is the speed of light, and f_{EY} is the dimensionless eclipse–Yarkovsky coefficient. The angle ψ is the inclination of the ring plane with respect to the heliocentric orbital plane. If the ring has a dynamical optical depth τ and the Sun stands at elevation ψ above the ring plane, the ray path through the particle layer is lengthened by $1/\sin\psi$, giving a suppression factor $e^{-\tau/\sin\psi}$ of the radiation flux. In fact, we have $\sin\psi = \sin\varepsilon_p|\cos\lambda|$ where ε_p is the planet's obliquity (e.g., $\varepsilon_p \simeq 26^{\circ}\!.7$ for Saturn) and λ is the orbital longitude (starting with $\lambda = 0$ at a solstice). The planet's obliquity could evolve due to planetary perturbation (e.g., W. R. Ward 1973; D. P. Hamilton & W. R. Ward 2004; W. R. Ward & D. P. Hamilton 2004; M. Saillenfest et al. 2021; M. Ćuk et al. 2024), which is ignored in this Letter for simplicity. The ring is assumed to be located in the planet's equatorial plane.

In general, f_{EY} is a complex function of the rotation state, represented by the spin frequency ω and the obliquity ε (i.e., the angle between the particle spin vector and the pole of the orbit of the particle around the planet), the thermal properties, planet radius r_p, particle radius r, and stellar irradiance. The full solution of the EY coefficient obtained from solving the 3D heat conduction equation for a spherical particle can be subdivided into the planetary diurnal component $f_{\mathrm{EY,d}}$ (caused by the spin) and the planetary seasonal component $f_{\mathrm{EY,s}}$ (caused by the planetocentric orbit) (W.-H. Zhou et al. 2024):

$$f_{\mathrm{EY}} = f_{\mathrm{EY,d}} + f_{\mathrm{EY,s}}, \tag{10}$$

where

$$f_{\mathrm{EY,d}} = \frac{4}{9}\eta_{\mathrm{shadow}}\left[V(z_{\gamma-1})\cos^4\frac{\varepsilon}{2} - V(z_{\gamma+1})\sin^4\frac{\varepsilon}{2}\right], \tag{11}$$

$$f_{\mathrm{EY,s}} = -\frac{2}{9}\eta_{\mathrm{shadow}}V(z_1)\sin^2\varepsilon. \tag{12}$$

Here $\gamma = \omega/\Omega$, $z_x = \sqrt{-\imath x}\ r/r_\Omega$, and $\imath \coloneqq \sqrt{-1}$. The fraction of time in the shadow η_{shadow} averaged over the planetocentric and heliocentric orbits can be approximated as

$$\eta_{\mathrm{shadow}} = 0.5\left(\frac{R}{r_p}\right)^{-2.1}, \tag{13}$$

for $\varepsilon_p = 26^{\circ}\!.7$ in Saturn's case, which is validated in Appendix A. The thermal penetration depth over an orbit is $r_\Omega = \sqrt{K/(\rho C \Omega)}$ where K and C are the thermal conductivity and the specific heat capacity. We set the thermal conductivity $K = 10^{-4}\ \mathrm{W\,m^{-2}\,K^{-1}}$ and the specific heat capacity $C = 820\ \mathrm{J\,K^{-1}\,kg^{-1}}$ (D. Vokrouhlický et al. 2007). Finally $V(z)$ is a real-valued function defined by

$$V(z) = \mathrm{Im}\left(1 + \chi\frac{z}{j_1(z)}\frac{dj_1(z)}{dz}\right)^{-1} \tag{14}$$

with $j_1(z)$ denoting the spherical Bessel function of the first kind and order 1,

$$j_1(z) = \frac{\sin z}{z^2} - \frac{\cos z}{z}. \tag{15}$$

The variable χ is defined as

$$\chi = \frac{K}{\sqrt{2}\,r\epsilon\sigma T_{\mathrm{sub}}^3(1 - r_p/\pi R)^{3/4}}. \tag{16}$$

Here ϵ is the emissivity of the particle, $\sigma = 5.67 \times 10^{-8}\ \mathrm{W\,m^{-2}\,K^{-4}}$ is the Stefan–Boltzmann constant, η is the thermal inertia, and $T_{\mathrm{sub}} = ((1 - A_v)\Phi_s/\epsilon\sigma)^{1/4}$ is the subsolar temperature, with A being the albedo.

For the sake of easier integration, we approximate the dependence of f_{EY} on the particle radius r as

$$f_{\mathrm{EY}} = \begin{cases} f_{\mathrm{EY,0}}, & r \geqslant r_0, \\ f_{\mathrm{EY,0}}\ (r/r_0)^3, & r < r_0, \end{cases} \tag{17}$$

where $f_{\mathrm{EY,0}}$ is only independent of r, but still depends on other parameters such as rotational and thermal properties. Here $r_0 \sim r_\Omega \sim 1$ mm is the characteristic thermal penetration depth, below which the thermal wave penetrates the body so that the surface temperature tends to be more uniform for smaller particles. A detailed justification for this approximation is provided in Appendix B. Equation (17) is based on the assumption that particles of all sizes have the same rotation state. However, when we consider a ring system, we need to account for the size-dependent rotational distribution. We will show in Section 4 that, even under a realistic rotational distribution in different size ranges, the approximation in Equation (17) remains valid for estimating the total EY torque on the ring.

For a layer of ring annulus where the optical depth is between τ' and $\tau' + \Delta\tau'$ at radius R, the total number of particles in this layer is $N\Delta\tau'/\tau$ where $\tau = \sum_i \pi r_i^2\Sigma/m_i$ is the dynamical optical depth and $N = 2R\Delta R\,\tau/r^2$ is the total number of particles in the annulus. The total torque exerted by the EY effect on all particles at the layer is given by

$$T_{\mathrm{EY}} = \sum_i F_{\mathrm{EY},i}R = \frac{(1 - A_v)\,\Phi_s R}{c}\,e^{-\tau'/\sin\psi}\sum_i \pi r_i^2 f_{\mathrm{EY},i}, \tag{18}$$

where the sum is taken over all particles in the annulus. We begin by assuming that all ring particles have the same radius r, in which case the torque simplifies to

$$\begin{aligned} T_{\mathrm{EY}} &= \frac{(1 - A_v)\,\Phi_s R}{c}\,e^{-\tau'/\sin\psi}\,\frac{N\Delta\tau'}{\tau}\pi r^2\bar{f}_{\mathrm{EY}} \\ &= \frac{(1 - A_v)\,\Phi_s R}{c}\,e^{-\tau'/\sin\psi}\,2\pi R\Delta R\Delta\tau'\bar{f}_{\mathrm{EY}}. \end{aligned} \tag{19}$$

The quantity $\bar{f}_{\mathrm{EY}} \coloneqq \sum_i f_{\mathrm{EY},i}/N$ is the mean eclipse–Yarkovsky coefficient for particles of radius r, which accounts for variation in spin states across the particle population. The total EY torque is the integral over τ' from 0 to τ:

$$\begin{aligned} T_{\mathrm{EY}} &= \int_0^\tau 2\pi R^2\Delta R\,\frac{(1 - A_v)\,\Phi_s\bar{f}_{\mathrm{EY}}}{c}\,e^{-\tau'/\sin\psi}d\tau' \\ &= 2\pi R^2\Delta R\frac{(1 - A_v)\,\Phi_s\bar{f}_{\mathrm{EY}}}{c}(1 - e^{-\tau/\sin\psi})\sin\psi. \end{aligned} \tag{20}$$

For an extremely tenuous ring with $\tau \ll 1$, $T_{\mathrm{EY}} \sim 2\pi R^2\Delta R(1 - A_v)\,\Phi_s\bar{f}_{\mathrm{EY}}\tau/c$, indicating the total torque is proportional to the total area of ring particles in the annulus $2\pi R\Delta R\tau$. On the other hand, for a dense ring with $\tau \gg 1$, $T_{\mathrm{EY}} \sim 2\pi R^2\Delta R(1 - A_v)\,\Phi_s\bar{f}_{\mathrm{EY}}\sin\psi/c$, indicating the total torque is proportional to the projected area of the ring $2\pi R\Delta R \sin\psi$. Interestingly, when $r > r_0 \simeq 1$ mm, the total torque does not depend on particle size since the mean EY torque efficiency $\bar{f}_{\rm EY} = \bar{f}_{\rm EY,0}$, which is independent of the size according to Equation (17).

In reality, ring particles follow a certain SFD, often approximated with a power law (e.g., N. Brilliantov et al. 2015). To account for this, we replace $\bar{f}_{\rm EY}$ with a size-free variable $\bar{f}_{\rm EY,0}$, and encapsulate the size effects into a dimensionless size correction factor $\eta_{\rm size}$. The torque then becomes

$$T_{\rm EY} = 2\pi R^2 \Delta R\, \frac{(1 - A_{\rm v})\,\Phi_{\rm s} \bar{f}_{\rm EY,0}\, \eta_{\rm size}}{c}\, (1 - e^{-\tau/\sin\psi}) \sin\psi, \tag{21}$$

where the detailed expression for $\eta_{\rm size}$ is provided in Appendix C. In fact, when the considered minimum size $r_{\rm min} > r_0 \sim 1$ mm, we have $\eta_{\rm size} = 1$ regardless of the SFD. When $r_{\rm min} < r_0$, we have $\eta_{\rm size} < 1$. A typical power-law differential size–frequency distribution follows $dN \propto r^{-\alpha}$ with $-\alpha$ being the power index. As shown in Appendix C, $\eta_{\rm size}$ is dominated by the largest particles for shallow size–frequency distributions ($\alpha < 3$) and by the smallest particles for steep distributions ($\alpha > 3$). At the critical slope $\alpha = 3$, contributions from both large and small particles are significant. Cassini observations suggest that α in Saturn's main rings spans the range $2.7 \lesssim \alpha \lesssim 3.2$ (see review by K. E. Miller et al. 2024). In this study, we adopt $\alpha = 3$, which is also supported by theoretical expectations (N. Brilliantov et al. 2015).

Since ψ vary with time over the solar seasons, the factor $(1 - e^{-\tau/\sin\psi})\sin\psi$ should be averaged over λ to calculate the secular effect of the EY torque. While the average of $\sin\psi$ is exactly $\frac{2}{\pi}\sin\varepsilon_{\rm p}$, that of the full expression does not lead to a closed-form expression in elementary functions. We offer the following approximation, correct to within less than 2%:

$$\begin{aligned} g(\tau, \varepsilon_{\rm p}) &= \langle (1 - e^{-\tau/\sin\psi})\sin\psi \rangle \\ &\approx (1 - e^{-\tau/(2\sin\varepsilon_{\rm p}/\pi)})\frac{2\sin\varepsilon_{\rm p}}{\pi} \times G(\tau, \varepsilon_{\rm p}), \end{aligned} \tag{22}$$

where G is a fitting function of order unity:

$$G(\tau, \varepsilon_{\rm p}) = 1 - 2ue^{-u}/7 \tag{23}$$

with

$$u = \tau \times \left(\frac{100}{\varepsilon_{\rm p}[\rm deg]} + \frac{\varepsilon_{\rm p}[\rm deg]}{150} \right). \tag{24}$$

Note that for all τ and $\varepsilon_{\rm p}$, $0.89 < G(\tau, \varepsilon_{\rm p}) \leqslant 1$; in other words, discarding G degrades the fit by $\sim$10%.

Including the EY torque $T_{\rm EY}$ in the angular momentum conservation equation (Equation (7)) and taking the limit $\Delta R \to 0$, we arrive at

$$\begin{aligned} &\tfrac{\partial}{\partial t}(\Sigma R^2 \Omega) + \tfrac{1}{R}\tfrac{\partial}{\partial R}(\Sigma R^3 \Omega v_R) \\ &\quad = -\tfrac{3}{2R}\tfrac{\partial}{\partial R}(\nu \Sigma R^2 \Omega) \\ &+ \tfrac{R(1 - A_{\rm v})\,\Phi_{\rm s}}{c}\, \bar{f}_{\rm EY,0}\, \eta_{\rm size}\, g(\tau, \varepsilon_{\rm p}). \end{aligned} \tag{25}$$

Combining Equations (4) and (25), and two factors η_τ and $\eta_{\rm p}$ that will be introduced in Sections 3.2 and 3.3, we obtain the modified surface density evolution equation including the EY effect:

$$\begin{aligned} \frac{\partial \Sigma}{\partial t} = \frac{3}{R}\frac{\partial}{\partial R}\left(\sqrt{R}\frac{\partial}{\partial R}(\nu \Sigma \sqrt{R}) \right) \\ - \frac{2(1 - A_{\rm v})\,\Phi_{\rm s} \eta_{\rm size}}{cR}\, \frac{\partial}{\partial R}\left(\frac{\bar{f}_{\rm EY,0} R\, \eta_\tau\, \eta_{\rm p}\, g(\tau, \varepsilon_{\rm p})}{\Omega} \right). \end{aligned} \tag{26}$$

Here $f_{\rm EY,0}$ scales as $R^{-2.1}$ for $\varepsilon_{\rm p} = 26\overset{\circ}{.}7$ (Equation (13)). Note that even in the case $\eta_{\rm size} = 1$, the particle size r is still relevant in Equation (26), as r emerges from $\tau \sim 3\Sigma/4\rho r$ in the EY term. Generally, the EY effect is inversely proportional to the particle size. The value of $f_{\rm EY,0}$ will be determined in Section 4.

3.2. Consideration of High Optical Depth

The analytic expressions for the EY effect (Equations (10), (11), and (12)) are derived under the assumption that each ring particle maintains a constant shape and spin state over the course of an orbital period. This assumption may be violated in dense regions of the ring, where high optical depths allow for frequent interparticle collisions and the formation of transient nonspherical aggregates. To account for this, we introduce a conservative attenuation scheme to justify the implementation of the EY torque under such conditions.

In regions of high optical depth, ring particles can temporarily self-aggregate due to self-gravity and cohesion (e.g., R. P. Perrine & D. C. Richardson 2012), forming gravitational wakes, which are unstable, anisotropic structures that persist for roughly an orbital timescale. These wakes violate the assumption of spherical, isolated particles and significantly alter both the effective shape and the emission geometry, which are critical for the EY effect. Since the analytic EY solution assumes a rigid, spherical body, its application becomes questionable in the presence of gravitational wakes. A common stability criterion for wake formation is the Toomre parameter $Q > 2$ where

$$Q = \frac{\Omega v_R}{3.36\, G\Sigma}, \tag{27}$$

where v_R is the radial velocity dispersion. Substituting $v_R \sim \sqrt{Gm/r}$ and using the standard definition of optical depth $\tau = 3\Sigma/(4\rho r)$, we obtain

$$\tau < \frac{\rho_{\rm p}}{\rho}\frac{\sqrt{4\pi G\rho/3}}{\Omega}, \tag{28}$$

where $\rho_{\rm p}$ is the bulk density of the planet and ρ is the bulk density of ring particles. As an illustrative example, let us consider Saturn's A ring. Taking Saturn's density $\rho_{\rm p} = 687\,{\rm kg\,m^{-3}}$, particle density $\rho = 1000\,{\rm kg\,m^{-3}}$, and orbital period $2\pi/\Omega \approx 10\,{\rm hr}$, we find $\tau < 2$, which is representative of typical planetary ring conditions.

In addition, rotation may be changed by collisions before the particle completes an orbital period in the dense ring. Since the EY torque depends sensitively on a particle's rotation, the analytic expressions are only valid if the rotation state remains approximately constant during an orbit. While a fully time-variable spin might still produce a net EY torque, such behavior is beyond the scope of this work. To constrain this regime, we estimate the average number of collisions per particle per orbit as $4\pi\tau$. Since each collision would change the rotation of two particles, requiring fewer than one spin change per orbit per particle yields a critical optical depth of $\sim 1/8\pi \simeq 0.05$.

Although a full treatment of EY dynamics under frequent collisions and wake-dominated conditions is deferred to future work, we conservatively model the suppression of the EY effect at high τ by multiplying by a smooth attenuation function:

$$\eta_\tau = \begin{cases} 1, & \tau \leqslant \tau_1 \\ (\tau_2 - \tau)/(\tau_2 - \tau_1), & \tau_1 < \tau < \tau_2 \\ 0 & \tau \geqslant \tau_2. \end{cases} \tag{29}$$

This function captures the gradual decay of EY effectiveness with increasing optical depth and serves as a practical approximation in the absence of a full numerical model. In the illustrative examples in this Letter, we adopt $\tau_1 = 1/8\pi \sim 0.05$ and $\tau_2 = 2$ for estimation.

Note that the suppression of the EY effect at high τ does not imply that the EY effect is dynamically irrelevant in dense rings. In fact, the EY effect remains active at the ring edges where the optical depth is low, so it can influence the overall angular momentum transport and thereby the global evolution of dense rings, as demonstrated in Section 5.

3.3. Consideration of Planetary Radiation

Planetary radiation incident on the ring particle can produce an effect opposite to the EY effect (D. P. Rubincam 2006; D. Vokrouhlický et al. 2007; W.-H. Zhou et al. 2024), which is termed the "Yarkovsky–Rubincam effect" (P. Farinella & D. Vokrouhlický 1996), "Rubincam effect" (M. Ćuk & J. A. Burns 2005), or "planetary–Yarkovsky effect" (D. Vokrouhlický et al. 2007). It has been shown (D. P. Rubincam 2006; D. Vokrouhlický et al. 2007) that the ratio between the thermal force caused by the planetary radiation and that from the EY effect can be written as

$$\mathcal{F} = \frac{\bar{\Phi}_{\mathrm{p}}}{(1 - A_{\mathrm{v}})\, \Phi_{\mathrm{s}}\, \eta_{\mathrm{shadow}}(R, \varepsilon_{\mathrm{p}})\, g(\tau, \varepsilon_{\mathrm{p}})}. \tag{30}$$

where $\bar{\Phi}_{\mathrm{p}}$ is the planetary radiation flux on the ring particle. Interestingly, $\mathcal{F}$ is independent of particle properties, depending solely on the geometry of the ring. This ratio yields a reduction factor $\eta_{\mathrm{p}} = 1 - \mathcal{F}$ to f_{EY} (Equation (26)), with $\eta_{\mathrm{p}} = 1$ representing zero planetary radiation. Note that η_{p} could be negative and reverse the total torque if the planetary radiation is sufficiently strong. The effect of planetary radiation can be strengthened if (1) the ring particle's albedo in the wavelength range of the planet's thermal emission is low, which means the particle absorbs more radiation from the planet, or (2) the planet emits more radiation than it receives due to the release of internal energy.

In the following, we calculate $\bar{\Phi}_{\mathrm{p}}$, the radiation received by a ring particle at the orbital distance R with normal (dynamical) optical depth τ. As the ring is separated from the planet by just a few planetary radii, the planet cannot be treated as a point source but needs to be decomposed into surface elements ΔS_p. We assume the planet emits as a Lambertian surface of radiance L.

The position vector of the ring particle is $\boldsymbol{R}$ and the position vector of the arbitrary planetary surface element is $\boldsymbol{r}_{\mathrm{p}} = r_{\mathrm{p}}\, \hat{n}_{\mathrm{p}}$, where $\hat{n}_{\mathrm{p}}$ is both the outward surface normal and a unit vector on the sphere. The vector from the planet surface element to the ring point is

$$\boldsymbol{s} = \boldsymbol{R} - \boldsymbol{r}_{\mathrm{p}}, \tag{31}$$

and the unit vector is $\hat{\boldsymbol{s}} = \boldsymbol{s}/s$. A planetary surface element contributes only if it is visible from the ring point. This requires the Lambert emission cosine

$$\mu_{\mathrm{p}} \equiv \hat{n}_{\mathrm{p}} \cdot \hat{\boldsymbol{s}} > 0. \tag{32}$$

Under this condition, the differential absorbed flux at a ring point, per unit ring midplane area, is

$$\Delta\Phi_{\mathrm{abs}} = L\, \mu_{\mathrm{p}}\, \frac{\Delta S_p}{s^2} \sin\psi_{\mathrm{p}}\, (1 - e^{-\tau/\sin\psi_{\mathrm{p}}}), \tag{33}$$

Here, ψ_{p} is the elevation angle of radiation from the planetary surface element as seen from the ring plane (the same consideration as the starlight elevation angle ψ in Equation (20)), which is defined as

$$\sin\psi_{\mathrm{p}} = |(-\hat{s}) \cdot \hat{n}_{\mathrm{ring}}|, \tag{34}$$

where $\hat{n}_{\mathrm{ring}}$ is the normal vector of the ring plane, equal to the spin axis of planet.

Let us now estimate L. Assuming the absorbed stellar flux is redistributed uniformly over the planet and reemitted thermally, one gets for the thermal emission

$$L_{\mathrm{IR}} = \frac{\Phi_{\mathrm{s}}(1 - A_p)}{4\pi}\Xi \tag{35}$$

where the factor of $1/4$ comes from the uniform emission of the received radiation ($\pi r_{\mathrm{p}}^2/4\pi r_{\mathrm{p}}^2$), $1/\pi$ is the radiant intensity (i.e.,power per unit solid angle) from A_p is the albedo of the planet in the visible, and Ξ is a factor accounting for the fact that the planet may emit more power than it receives from sunlight due to the release of internal energy. Moreover, the planet reflects the visible light: $L_v = \Phi_s A_p/4$ on average over the surface.

Assuming the particle has a visible albedo A_{v} and an albedo A_{IR} in the planet's emission band, the total radiation absorbed by the particle is $(1 - A_{\mathrm{v}})L_v + (1 - A_{\mathrm{IR}})L_{\mathrm{IR}} = (\Phi_s/4)[A_{\mathrm{p}}(1 - A_{\mathrm{v}}) + \Xi(1 - A_{\mathrm{p}})(1 - A_{\mathrm{IR}})]$. Therefore, Equation (33) can be expanded as

$$\begin{aligned} \Delta\Phi_{\mathrm{abs}} = {} & \tfrac{\Phi_{\mathrm{s}}}{4\pi}\, \mu_{\mathrm{p}}\, \tfrac{\Delta S_{\mathrm{p}}}{s^2} \sin\psi_{\mathrm{p}}\, (1 - e^{-\tau/\sin\psi_{\mathrm{p}}}) \\ & \times [A_{\mathrm{p}}(1 - A_{\mathrm{v}}) + \Xi\, (1 - A_{\mathrm{p}})(1 - A_{\mathrm{IR}})]. \end{aligned} \tag{36}$$

The total planetary flux absorbed by the ring particle is then $\bar{\Phi}_{\mathrm{p}} = \iint \Delta\Phi_{\mathrm{abs}}$. The area of the surface element is $\Delta S_{\mathrm{p}} = r_{\mathrm{p}}^2 \sin\theta_{\mathrm{p}} \Delta\theta_{\mathrm{p}} \Delta\phi_{\mathrm{p}}$ with θ_{p} and ϕ_{p} the colatitude and azimuthal angles, respectively. The surface integral is most conveniently evaluated numerically using Monte Carlo uniform sampling on the planet's surface. Noting

$$h(R, \tau) = \iint \frac{\mu_{\mathrm{p}}}{4\pi s^2} \sin\psi_{\mathrm{p}}\, (1 - e^{-\tau/\sin\psi_{\mathrm{p}}})\Delta S_p, \tag{37}$$

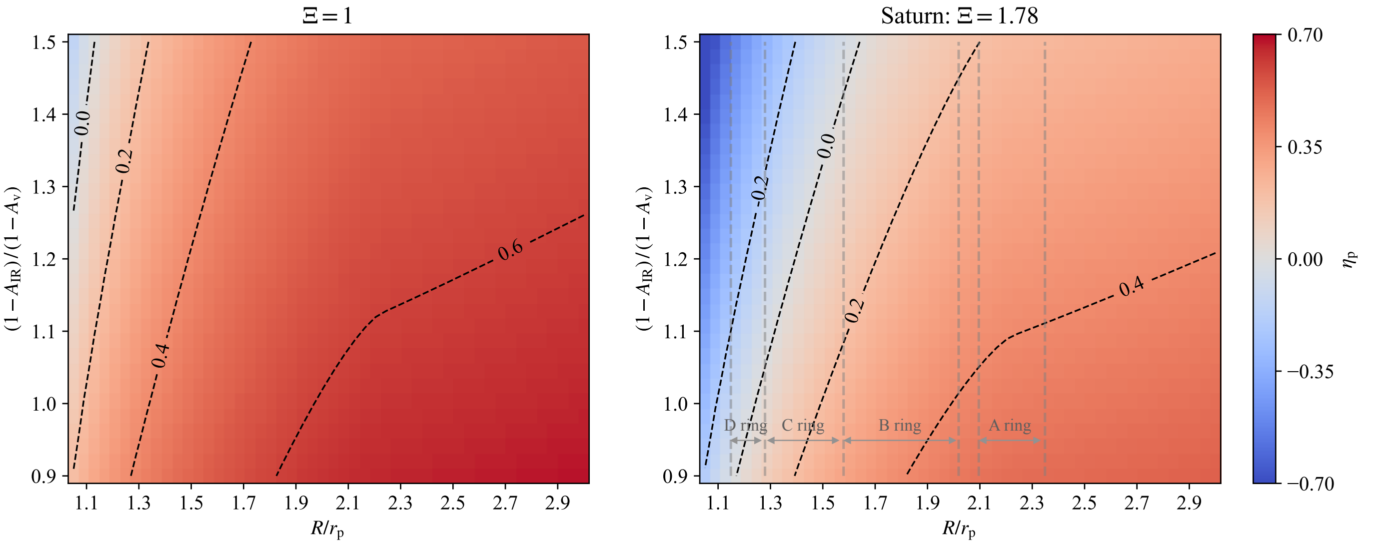

Figure 3. The factor η_p due to the planetary radiation as a function of the orbital distance R and $(1 - A_{IR})/(1 - A_v)$ (a higher value represents a greater influence of planetary radiation), considering different emissivities of the planet, $\Xi = 1$ (e.g., Martian case) and 1.78 (Saturn's case). The emissivity can partially come from the internal energy of the planet. For comparison among results obtained with different values of Ξ, we fix the planetary obliquity at $\varepsilon_p = 25°$, representative of both Mars (25°.2) and Saturn (26°.7). The planet's albedo is set as $A_p = 0.342$. For Saturn's rings, previous works adopt $(1 - A_{IR})/(1 - A_v) = 1.33$ for A/B rings (D. P. Rubincam 2006; D. Vokrouhlický et al. 2007), while A_{IR} is highly uncertain.

the ratio $\mathcal{F}$ becomes

$$\mathcal{F} = \frac{h(R, \tau)}{\eta_{\rm shadow}(R, \varepsilon_p) g(\tau, \varepsilon_p)} \frac{A_p(1 - A_v) + \Xi(1 - A_p)(1 - A_{IR})}{1 - A_v}. \tag{38}$$

Figure 3 shows the factor $\eta_p = 1 - \mathcal{F}$ as a function of the orbital distance R and $(1 - A_{IR})/(1 - A_v)$, accounting for $\Xi = 1$ (Martian case) and $\Xi = 1.78$ (Saturn's case). The optical depth τ is set to be 0.1 and the obliquity is 25°. Generally, η_p decreases as $(1 - A_{IR})/(1 - A_v)$ increases, since this ratio represents the ratio of the ability to absorb the thermal radiation from the planet to the ability to absorb the visible radiation from the Sun. On the other hand, η_p increases as R increases, since the planet becomes more like a point source whose radiation is heavily suppressed by self-shadowing such that only the inner edge is illuminated.

For Saturn, the Bond albedo A_p is 0.342 and the emissivity Ξ is 1.78, which results in an emission flux of 4.4 W m^{-2} from Saturn's surface with the solar flux at Saturn $\Phi_s = 15.0$ W m^{-2}. The visible albedo of Saturn's rings A_v varies among the major rings: 0.5–0.6 for A and B icy ring particles (R. Morishima et al. 2010) and 0.2–0.3 for the C ring (C. Porco et al. 2005; L. J. Spilker et al. 2018). On the other hand, the thermal albedo at Saturn's emission peak (∼30 μm) is poorly constrained for Saturn's rings (see review by K. E. Miller et al. 2024). Previous studies adopt $A_{IR} = 0.335$, which yields $(1 - A_{IR})/(1 - A_v) = 1.33$ for A and B rings (D. P. Rubincam 2006; D. Vokrouhlický et al. 2007). In the Martian case, where $\Xi \simeq 1$, the ring predominantly migrates outward unless the ring particles possess an exceptionally high visible-to-thermal albedo ratio.

Another planetary source of radiation flux arises from the mutual heating of ring particles. In a ring with a random spatial distribution, this heating is approximately isotropic, which marginally elevates the mean particle temperature without significantly altering the surface temperature gradient. Consequently, under these assumptions, mutual heating does not introduce new thermal dynamics but simply shifts the mean temperature. While a more sophisticated model might move beyond the assumption of isotropy by accounting for specific particle coordinates, such analysis lies outside the scope of this study and is left for future investigation.

4. Numerical Determination of the EY Coefficient

The direction and magnitude of the EY torque are represented by the mean dimensionless EY coefficient $\bar{f}_{\rm EY,0}$ (Equation (21)) of ring particles, which depends on the rotational states (i.e., ω and ε, Equations (11) and (12)).

The rotational distribution of particles is dominated by the rotational energy exchange between particles during mutual collisions (e.g., H. Salo 1995; R. Morishima & H. Salo 2004; K. Ohtsuki 2005, 2006a, 2006b). Considering the rotational energy $E_{\rm rot} \propto r^5\omega^2$, the equipartition of rotational energy among particles tends to cause the spin rate to decrease with size as $\omega \propto r^{-2.5}$. However, the spin rate is determined by the balance of two effects during collisions: (1) collisional stirring, which transfers kinetic energy from random translational motion to rotational motion during collisions, tending to spin up smaller particles, with the spin rate scaling as $\omega \propto r^{-2.5}$; and (2) rotational friction, which describes the dissipation of relative spin motions between colliding particles through frictional torques, tending to suppress differences in spin and produce a spin rate that is nearly independent of particle size. The combination of these two effects leads to a spin rate scaling as $\omega \propto r^{-1}$ (K. Ohtsuki 2005). Given a size distribution following a power law $dN \propto r^{-\alpha}$ with $\alpha = 3$, the mean spin rate follows

$$\bar{\omega} \sim \Omega \left(\frac{r}{0.5\, r_{\rm max}}\right)^{-1}, \tag{39}$$

with the maximum radius of the rings $r_{\rm max}$ being an arbitrary value (K. Ohtsuki 2005). On the other hand, the obliquities are random without any dependence on size.

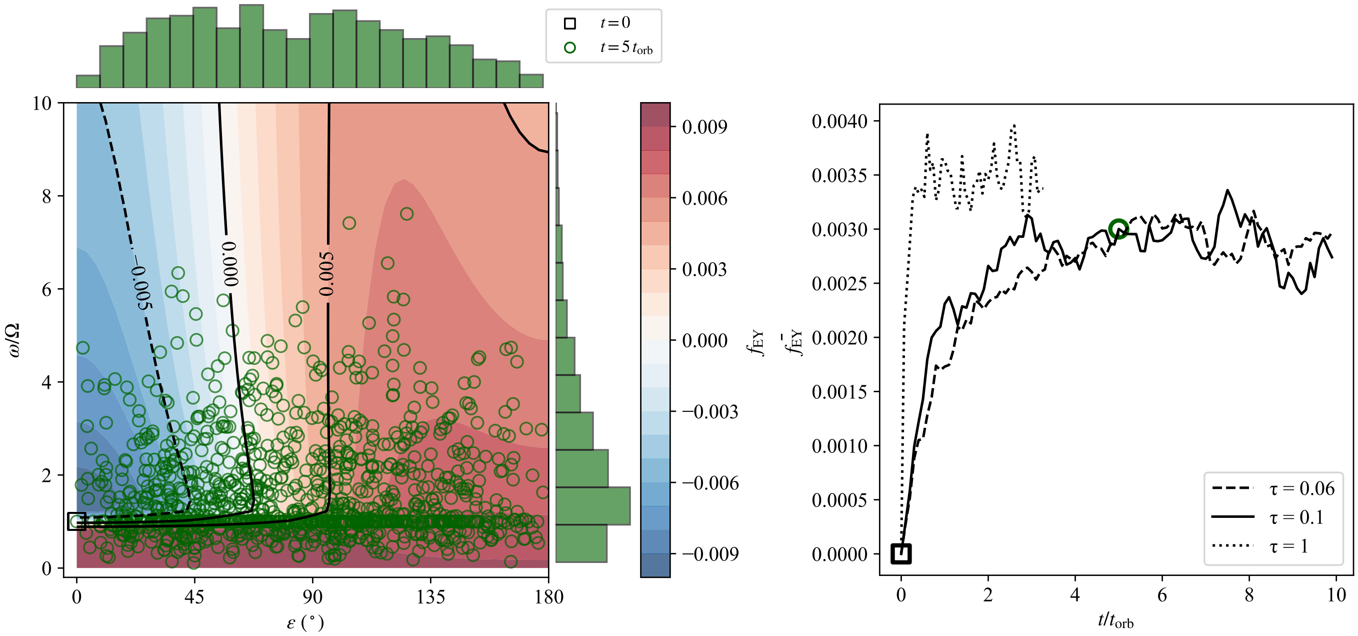

Figure 4. Illustration of the EY effect on the ring particles, taking the example of the Saturn system. These ring particles are located at 2 Saturn radii, with a thermal inertia of 10 tiu. The particle size ranges from 0.7 m to 2.3 m, distributed according to a power law with a power index of −3. The left panel shows the distribution of rotation (i.e., the spin rate ω and the obliquity ε) of ring particles at $t = 0$ (black square) and $t = 5t_{\rm orb}$ (green circles). The colors in the background denote the values of $f_{\rm EY}$. The right panel shows the convergence of the EY coefficient $f_{\rm EY}$ over time with the epochs in the left panel included, considering different optical depths τ. This indicates that we can simply adopt a constant $\bar{f}_{\rm EY}$ for the long-term evolution.

To obtain the statistical distribution of ω and ε, we performed simulations of planetary rings using the `pkdgrav` gravitational N-body code (D. C. Richardson et al. 2000; J. G. Stadel 2001; R. P. Perrine & D. C. Richardson 2012). Particle collisions were modeled using the soft-sphere discrete element method (SSDEM), in which particles can overlap as a proxy for surface deformation. The contact forces between overlapping particles are determined by the degree of overlap and the contact history using a spring dash-pot model, where reaction forces and torques are determined by a user-specified spring constant in Hooke's law (related to the material stiffness), damping parameters (related to the coefficient of restitution), and coefficients of static, rolling, and twisting friction (S. R. Schwartz et al. 2012; Y. Zhang et al. 2017). The SSDEM model allows for realistic modeling of low-speed collisions with finite contact durations, dissipation (via friction), and angular momentum transfer. The simulations are performed in the comoving Hill frame for a small "patch" of ring particles. Self-gravity is included through the use of periodic boundary conditions with "ghost" particles that interact gravitationally with the patch. We refer the reader to R. P. Perrine et al. (2011) or R.-L. Ballouz et al. (2017) for a detailed description of `pkdgrav`'s implementation of planetary rings.

The particle sizes are assumed to follow a differential power-law SFD with an index of $\alpha = 3$. The ratio of maximum to minimum size is set to be $r_{\rm max}/r_{\rm min} = 3$ to reduce the computational cost of the nearest-neighbor search. Therefore, the expected mean spin rate is $\bar{\omega} \sim \Omega$ according to Equation (39).

Figure 4 shows an example of the evolution of the rotational distribution of ring particles in the Saturn system, with the parameters listed in Appendix D. The particles are assumed to have a mean radius of 1 m and be located at $R = 2r_{\rm p}$. The initial condition for every particle is $\omega = \Omega$ and $\varepsilon = 0$, for which the EY effect disappears. It can be seen that after a time $t =$ a few $t_{\rm orb} < t_{\rm col} = t_{\rm orb}/\tau$, the rotational distribution (left panel) and the mean EY coefficient $\bar{f}_{\rm EY,0}$ (right panel) evolve into equilibrium states. The EY coefficient $f_{\rm EY,0}$ of each particle is calculated with the complete formula in Appendix B and the assumed thermal properties. Typically, the spin rates normalized by the orbital frequency Ω follow a Maxwellian distribution peaked at 1, and the obliquities are distributed more evenly, consistent with the prediction of Equation (39). The material properties, such as the friction angle and restitution coefficient (Table 1), are adopted from asteroid studies (Y. Zhang & D. N. Lin 2020; Y. Zhang et al. 2022). Changing material properties may also influence the resulting spin distribution, which could be interesting to explore in future work. The EY coefficient converges to ∼0.003, as shown in Figure 4.

With this rotational distribution, we extrapolate the results down to particle sizes as small as 1 mm, according to Equation (39). Below this threshold, the EY effect diminishes rapidly and contributes negligibly to the total torque (Equation (17)). We found that the EY coefficient $f_{\rm EY}$ remains positive with a range from 3×10^{-3} to 9×10^{-3}. Therefore, we conclude that the total EY effect for ring particles following a realistic SFD is positive and we approximate it as $\sim 3 \times 10^{-3}$ for calculation in this Letter.

We also explore the rotational distribution and the resulting $\bar{f}_{\rm EY,0}$ by varying the optical depth, as shown in the right panel of Figure 4. We found that the rotational distribution remains the same, and $f_{\rm EY,0} \sim 0.003$ at $R = 2r_{\rm p}$ is independent of τ. This slight difference at $\tau = 1$ may be caused by the gravitational wake structures due to self-gravity. As we discussed in Section 3.1, the gravitational wake structure makes the presented EY estimate unreliable and would require new techniques to analyze. Therefore, combined with

Table 1
Simulation Parameters

Quantity	Symbol	Physical Value
Number of particles	N	1200
Number of SSDEM steps	N_{step}	339,411
SSDEM time step	Δt	1.2034 s
Spring constant	k_n	54.8108 kg s^{-2}
Central mass	M_{p}	5.7×10^{26} kg
Orbital distance	R	87,348 km
Orbital frequency	Ω	period = 7.36946 h
Patch width	W	220.149 m
Patch length	L	220.149 m
Patch thickness	H	10.7333 m
Mean particle radius	$\langle R \rangle$	1.07333 m
Mean particle mass	$\langle m \rangle$	1.4477×10^{4} kg
Mean Hill radius	$\langle r_{\mathrm{H}} \rangle$	$2.50682\langle R \rangle$
Mean escape speed	$\langle v_{\mathrm{esc}} \rangle$	$6.87457\Omega\langle R \rangle$
Optical depth	τ	0.1
Surface density	Σ	358.669 kg m^{-2}
Mean particle density	ρ_{s}	2 g cm^{-3}
Critical wavelength	λ_{crit}	20.0082 m
Friction angle	ϕ	35°
Normal restitution coefficient	ϵ_{n}	0.5
Tangential restitution coefficient	ϵ_{t}	0.5

Equation (13), $\bar{f}_{\mathrm{EY},0}$ can be approximated as

$$\bar{f}_{\mathrm{EY},0} = 0.003 \left(\frac{R}{2r_{\mathrm{p}}}\right)^{-2.1}, \tag{40}$$

which can be used in Equation (26) for solving the ring evolution.

We conclude that the net EY torque on the ring is positive, accounting for the rotational distribution of all ring particles undergoing collisions. Note that other factors such as the thermal properties and orbital radius only affect the magnitude and not the sign of $f_{\mathrm{EY},0}$ (see, e.g., Equations (11) and (12)). The outcome of the positive torque is not unexpected: both the seasonal component (Equation (12)) and the second term in the diurnal component (Equation (11)) are inherently positive, whereas the first term in the diurnal component can be either positive or negative. Therefore, since there are more positive components, their combined contribution would probably result in a net positive torque, which is also illustrated by the larger red area (positive f_{EY}) in Figure 4.

5. Long-term Evolution with the EY Effect

In this section, we investigate the long-term evolution of planetary rings with the viscous effect and the EY effect by numerically solving Equation (26) with a forward Euler method. We adopted zero surface density as the boundary conditions. As an illustration, we consider a synthetic Saturn-like system, that is, a planet with a mass of 5.7×10^{26} kg and an obliquity of 26°.7 with the ring lying in the equatorial plane. The particles are assumed to have equal sizes of 0.1 m, with a thermal inertia of 10 tiu [J m^{-2} K^{-1} s$^{-1/2}$]. For the purpose of illustrating the EY effect, we adopt $\Xi = 1$, $A_{\mathrm{p}} = 0.3$, and $(1 - A_{\mathrm{IR}})/(1 - A_{\mathrm{v}}) = 1$ for calculation of η_{p}. Note that the exact case for Saturn (i.e., $\Xi = 1.78$, $A_{\mathrm{p}} = 0.342$, and $(1 - A_{\mathrm{IR}})/(1 - A_{\mathrm{v}}) = 1.33$ will be discussed in Section 6.1). The viscosity can be approximated as (J. Salmon et al. 2010)

$$\nu = \begin{cases} 0.2\,[v_R^2\tau/\Omega(1 + \tau^2)] + r^2\Omega\tau, & Q \geqslant 2 \\ 1.4\,(r_{\mathrm{H}}^5 G^2\tau^2\rho^2/r^3\Omega^3) + r^2\Omega\tau, & Q < 2 \end{cases} \tag{41}$$

with $r_{\mathrm{H}} = (2m/3m_{\mathrm{p}})^{1/3}R$ being the mutual Hill radius of particles.

Figure 5 illustrates examples of ring evolution dominated by viscosity and by the EY effect, obtained by varying their relative strengths and the optical depth. The initial optical depth is assumed to follow a Gaussian profile. In the case where the EY torque can strongly affect the ring without considering any suppression (i.e., η_τ and $e^{-\tau/\sin\psi}$), the evolutionary paths can be classified into three modes, based on η_τ. These modes may be realized successively during the lifetime of a single ring as its surface density evolves.

Regime 1. Dense regime ($\tau_{\max} > \tau_2$). In regions where $\tau > \tau_2$, viscous transport dominates, driving material inward. However, this inward migration halts at the ring edge where $\tau < \tau_2$, as the EY torque becomes significant. At the edge, the positive EY torque pushes material outward until it is balanced by the opposing viscous torque that arises from particle accumulation. This interaction naturally produces a sharp edge. The overall evolution in this regime is thus characterized by an initial inward drift due to viscosity, followed by outward migration driven by the EY effect.

Regime 2. Transitional regime ($\tau_2 > \tau_{\max} > \tau_1$). In this intermediate regime, the EY effect is partially suppressed in regions with $\tau > \tau_1$, by both the factor η_τ (Equation (29)) and the exponential factor $e^{-\tau/\sin\psi}$ (Equation (9)). Consequently, the inner regions of the ring—where the EY torque remains more efficient—migrate outward more rapidly than the denser outer portions, producing a pronounced sharp inner edge. Meanwhile, the outer edge stretches outward as the region closer to it has a lower optical depth and thus moves faster. The global evolution is dominated by net outward migration driven by the EY effect.

Regime 3. Tenuous regime ($\tau_{\max} < \tau_1$). When the entire ring is optically thin, the EY effect operates efficiently throughout it. The result is a nearly uniform outward expansion of the ring without major distortion of its surface density profile.

Note that these three regimes are classified based on the suppression factor η_τ and the assumption that the EY effect is stronger than the viscous effect given that the suppression factor η_τ is ignored. If, instead, the EY timescale is considerably longer than the viscous timescale, then the behavior characteristic of Regime 3 could also occur within a transitional ring or a tenuous ring, that is, the ring may first drift inward due to viscosity before reversing direction and migrating outward under the influence of the EY torque.

Overall, the principal outcome of the EY effect is to decrete the ring, driving material outward, rather than to accrete it inward, as expected in the classical viscosity-dominated picture. The degree to which a planet decretes its ring depends on the strength of the EY torque relative to viscous transport and on the local optical depth conditions described by the three regimes above.

6. Applications and Discussion

The EY effect introduces a positive angular momentum flux over long-term evolution, which has important implications for the origin, structure, and dynamical age of ring systems. This

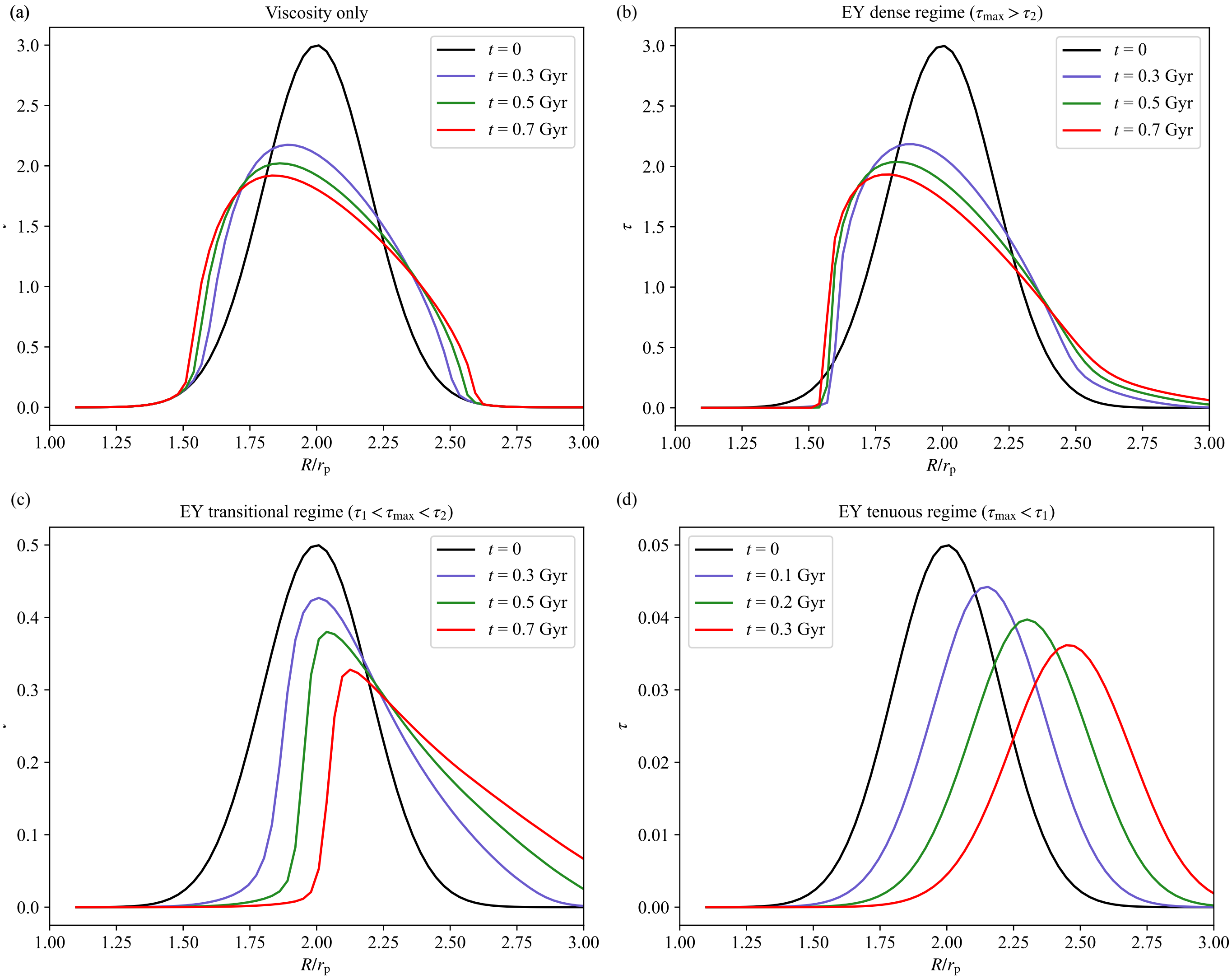

Figure 5. Examples of ring evolution for viscous evolution (a) and EY-included evolution in order of decreasing optical depth from (b) to (d). The simulation domain extends to $4r_p$, while the panels display to $3r_p$, corresponding to the commonly adopted fluid Roche limit. The rings are assumed to orbit Saturn, with a mean particle size of 0.1 m. Note the difference in y-axis scales between the panels.

includes both planetary rings and asteroidal rings observed in the solar system (e.g., F. Braga-Ribas et al. 2014; B. E. Morgado et al. 2023). We briefly discuss the applications to ring systems with examples of Saturn's rings and the Martian past ring.

6.1. Inner Sharp Edges of Saturn's Rings

Saturn's A and B rings display remarkably sharp inner and outer edges, which are not expected from viscous evolution. While the sharp outer edges are well explained by gravitational shepherding from nearby moons, the origin of the sharp inner edges remains an open question (see, e.g., A. Crida et al. 2025). One proposed solution is ballistic transport, in which high-speed micrometeoroid impacts redistribute mass inward and angular momentum outward from the inner edge, helping maintain a preexisting sharp inner edge (P. R. Estrada & R. H. Durisen 2023). However, the sharp inner edge itself cannot be created by the ballistic transport, implying a missing mechanism to initially produce it (P. R. Estrada & R. H. Durisen 2023; A. Crida et al. 2025).

As discussed in Section 5, both the EY transitional and dense regimes can spontaneously produce sharp inner edges. In particular, the shape of the edge of the bulk ring modeled in Figure 5 near $1.5r_p$ is reminiscent of the B–C ring transition. In addition, our simple model demonstrates that the inner sharp edge and overall surface density profile of the A ring can be qualitatively reproduced in the EY-dominated dense regime, as shown in Figure 6. For this illustrative simulation, we adopt a particle size of 0.1 m with optical depth thresholds $\tau_1 = 0.05$ and $\tau_2 = 2$. For the calculation of η_p, we adopt $\Xi = 1.78$, $A_p = 0.342$, and $(1 - A_{IR})/(1 - A_v) = 1.33$, following D. P. Rubincam (2006) and D. Vokrouhlický et al. (2007). The initial ring profile is assumed to follow a Gaussian distribution. As this is a simplified model including only viscosity and the EY effect, it does not capture the finer structural details caused by gravitational interactions with Saturn or its moons, which are beyond the scope of this study.

6.2. Long-term Evolution of Saturn's Rings

Traditional viscous spreading transports the majority of mass inward, but the EY torque may produce an outward drift

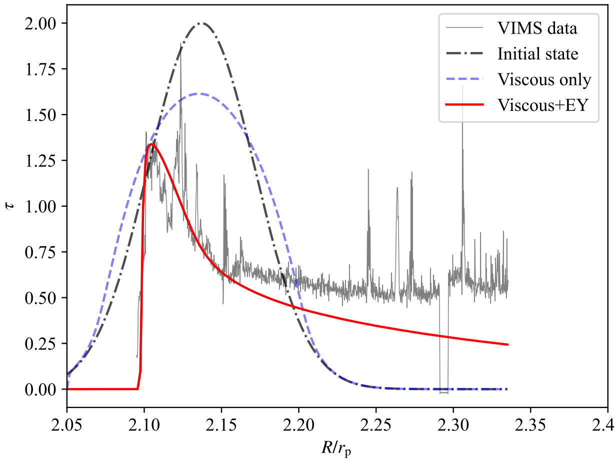

Figure 6. Evolution of Saturn's A ring with our model with only the viscous and EY effects included, in comparison with observed data. Here, the EY effect is estimated based on the particle size of 0.1 m and the particle thermal inertia of 10 tiu. The evolutionary time is 81 Myr. The initial τ profile is a Gaussian profile. The simulation domain extends to $2.4r_\mathrm{p}$, while the panel displays to $\sim 2.33r_\mathrm{p}$, to be consistent with the outer edge of the A ring confined by a 7:6 inner Lindblad resonance with Janus/Epimetheus.

of Saturn's main rings except for dense regions. Saturn's C and D rings could be exceptions, as they are so close to Saturn that the EY torque could even be reversed by planetary radiation (Figure 3). Determination of the direction of orbital evolution requires the precise value of the infrared albedo A_IR of particles in the C and D rings.

Saturn's D ring is optically very thin, $\tau < 10^{-3}$, and the particle sizes are believed to be 1–100 μm (M. M. Hedman et al. 2007). Hence, the Poynting–Robertson drag may dominate (D. Vokrouhlický et al. 2007; D. P. Rubincam 2013; R. Hyodo & S. Ida 2025) to drive materials inward, and the EY torque may be negligible.

In contrast, in the C ring, the particle sizes range from centimeters to meters (J. Cuzzi et al. 2009; M. M. Hedman et al. 2011), falling within the range where the EY effect is expected to be most efficient (i.e., larger than the thermal skin depth). The optical depth lies between 0.05 and 0.35, placing it within the tenuous or transitional regimes described in Section 5. Saturn's C ring is dynamically active and structurally complex, with structures such as the "plateaus" (e.g., R. G. French et al. 2017) whose origin is poorly understood. P. R. Estrada & R. H. Durisen (2023) suggest that C ring-like structures could emerge from the effects of micrometeoroid-driven ballistic transport (R. H. Durisen et al. 1989) onto the B ring. The EY torque may also interact with or counteract such an inward-acting process, potentially contributing to the formation. Therefore, the dynamical evolution and the resulting dynamical ages for Saturn's rings may require revisiting. These modifications to the standard dynamical model, including the interplay between EY torques and ballistic transport, will be explored in detail in a forthcoming companion study.

6.3. Formation of Planetary Moons

The EY effect introduces a novel pathway for satellite formation by enabling efficient outward angular momentum transport near ring edges. In classical models of viscous spreading, some ring material may diffuse across the Roche limit and gradually accumulate into moonlets (A. Crida & S. Charnoz 2012; M. Ciarniello et al. 2024; M. Blanc et al. 2025). However, in low-density rings, viscous torques are often too weak to drive substantial mass outward before the ring is lost to planetary accretion. The EY torque, by contrast, can act more efficiently in tenuous regions and accelerate the outward drift of particles toward the Roche limit, especially at ring boundaries.

This mechanism offers a fresh perspective on how ancient rings may dissipate and contribute to satellite formation. For example, A. J. Hesselbrock & D. A. Minton (2017) proposed a ring–moon cycling scenario for Mars, wherein rings repeatedly condense into moons that spiral inward and disrupt to form new rings. This model successfully reproduces the low mass and orbital characteristics of Phobos but predicts the existence of a coexisting tenuous ring, which has not been observed. A possible resolution is offered by the EY effect: the positive EY torque could expel the tenuous ring by pushing material beyond the Roche limit, facilitating its accretion onto Phobos.

G. Madeira et al. (2023) previously attempted to include the EY effect in this context but incorrectly modeled it as a negative torque. Our updated framework, incorporating the correct torque direction and magnitude, suggests that the EY effect may be a critical missing link in the completion of the ring–moon cycle. This scenario is the focus of a parallel study currently in preparation.

7. Conclusions

In this Letter, we have introduced and quantified the eclipse–Yarkovsky (EY) effect as a mechanism for the long-term dynamical evolution of planetary rings. This effect arises from the recoil force of ring particles due to asymmetric thermal emission following eclipse events, and its strength depends on particle size, thermal inertia, rotation state, and heliocentric distance. The underlying eclipse-modulated Yarkovsky torque has previously been explored primarily for individual objects in binary or satellite systems, such as Earth satellites and binary asteroids, where it is commonly referred to as the Yarkovsky–Schach effect. It has also been discussed in the context of Saturn's rings at the level of individual particles.

Here, we extend this effect to collisionally coupled planetary rings, which are treated as a continuous medium. Because interparticle collisions efficiently transport angular momentum between neighboring particles, the angular momentum input at the particle scale can be treated as a flux acting on the ring annulus as a whole. This allows the EY effect to be incorporated self-consistently into a continuum description of ring evolution. We derive the full surface density evolution equation including both viscous and EY torques (Equation (26)).

The planetary thermal radiation has an opposite effect to the EY effect, and its strength depends on the planet's albedo and internal energy release, as well as the ring particles' albedos in the visible and thermal wavelength ranges. We quantify this contribution by numerically integrating the radiation force from each emitting surface element of the planet, assuming Lambertian emission.

We validated the prescription for EY torque using rotational distributions obtained from N-body simulations by the code `pkdgrav`, showing that the EY effect produces a net positive angular momentum flux under typical conditions. Notably, we find that the total EY torque is independent of the particle size distribution and size range if the minimum size exceeds the thermal skin depth of ∼1 mm (but decreases with a decreasing size below the thermal skin depth). Instead, the total torque depends primarily on the ring's optical depth.

Based on the optical depth, we identify three evolutionary regimes: tenuous, transitional, and dense, depending on the optical depth. In the tenuous regime, the EY effect drives the whole ring outward with minor modification of the profile shape. In the transitional regime, the EY effect is gradually suppressed with increasing optical depth, leading to a sharp inner edge due to the stronger EY effect in the tenuous edge region. The global drift is outward. In the dense regime, the EY effect can be overpowered in the densest region, resulting in the dominance of the viscous evolution. The sharp inner edge can also be produced in the balance of the EY effect and viscosity. The overall evolution in this regime is a viscous spreading, followed by a net outward migration driven by the EY effect.

Our numerical results show that the EY effect could effectively drive Saturn's rings outward unless they are very close to Saturn (e.g., the location of the D ring), offering a new evolutionary pathway. Moreover, the EY effect spontaneously generates sharp inner edges, providing a natural explanation for features in Saturn's rings previously attributed solely to micrometeoroid-driven ballistic transport. Importantly, the EY effect may also contribute to satellite formation by facilitating material transfer across the Roche limit, with application to the formation of the Martian moons, which is under preparation in a parallel study. In conclusion, the EY effect is found to be a crucial mechanism affecting the formation, structure, and dynamical lifetimes of both planetary and asteroidal rings.

Acknowledgments

W.-H.Z. acknowledges support from the Japan Society for the Promotion of Science (JSPS) Fellowship (P25021). E.K. is supported by JSPS KAKENHI grants No. 24K00698. H.A. thanks CNES for support. The work of D.V. was supported by the Czech Science Foundation through grant 25-16507S. Numerical computations were carried out in part on the Licallo system at the Observatoire de la Côte d'Azur and on Cray XD2000 at the Center for Computational Astrophysics, National Astronomical Observatory of Japan.

Appendix A
The Fraction of Time in Shadow $\eta_{\rm Shadow}$

We numerically calculated the fraction of time in shadow for a particle at an orbital radius R. To determine whether a ring particle is in the planetary shadow, we compute the minimum distance between the center of the planet and the line connecting the particle and the Sun. The planet is placed at the origin with radius $r_{\rm p}$, and the unit vector of the solar direction is defined in the equatorial plane as

$$\hat{\boldsymbol{d}} = (\cos\phi, \sin\phi, 0), \tag{A1}$$

where ϕ is the heliocentric longitude of the Sun measured from the x-axis. The position of a ring particle on a circular orbit of radius R with an inclination $\varepsilon_{\rm p} = 26\overset{\circ}{.}73$ with respect to the heliocentric orbit is given by

$$\hat{\boldsymbol{R}}(\xi) = (\cos\xi,\ \cos\varepsilon_{\rm p}\sin\xi,\ \sin\varepsilon_{\rm p}\sin\xi), \tag{A2}$$

where ξ is the planetocentric true anomaly measured in the ring plane.

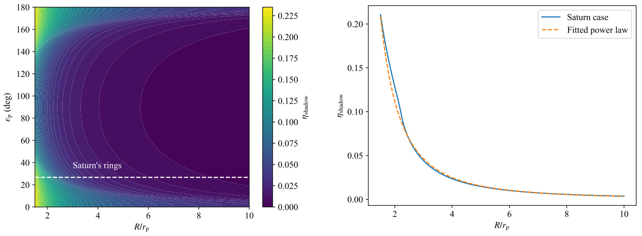

Figure 7. The fraction of time in shadow $\eta_{\rm shadow}$ as a function of the orbital radius R in Saturn's case where the planet obliquity is $\varepsilon_{\rm p} = 26\overset{\circ}{.}73$. The fitted function is $\eta_{\rm shadow} = 0.5\,(R/r_{\rm p})^{-2.17}$.

A shadow occurs when this line intersects the planetary sphere of radius $R_{\rm p}$. This is equivalent to requiring that the minimum distance between the line and the origin is smaller than $R_{\rm p}$,

$$\mathrm{dist}_{\min} = R\sqrt{1 - (\hat{\boldsymbol{R}}\cdot\hat{\boldsymbol{d}})^2} \leqslant r_{\rm p}, \tag{A3}$$

and that the intersection lies between the planet and the particle, i.e., along the line from the particle to the Sun,

$$\hat{r}\cdot\hat{\boldsymbol{D}} \leqslant 0. \tag{A4}$$

The combined condition becomes

$$\hat{R}\cdot\hat{d} \leqslant -\sqrt{1 - \left(\frac{r_{\rm p}}{R}\right)^2}. \tag{A5}$$

Substituting the explicit forms of $\hat{r}$ and $\hat{D}$, we obtain the condition

$$\cos\xi\cos\phi + \cos\varepsilon_{\rm p}\sin\xi\sin\phi \leqslant -\sqrt{1 - \left(\frac{r_{\rm p}}{R}\right)^2}. \tag{A6}$$

In the numerical algorithm, we set both ξ and ϕ uniformly in the interval $[0, 2\pi]$. For each pair (ξ_i, ϕ_j), we check whether it satisfies (A6). The total number of "shadowed" grid points, normalized by the total number of samples, gives the time-averaged shadow fraction:

$$\eta_{\rm shadow}(R) = \frac{1}{(2\pi)^2}\iint H\left[-\cos\xi\cos\phi - \cos\varepsilon_{\rm p}\times\sin\xi\sin\phi - \sqrt{1 - \left(\frac{r_{\rm p}}{R}\right)^2}\right] d\xi\, d\phi, \tag{A7}$$

where $H(x)$ is the Heaviside step function. This two-dimensional averaging procedure ensures that both the ring orbital motion and the planet's orientation relative to the Sun are accounted for.

Then we fitted the numerically obtained shadow fractions with a power-law function of the form

$$\eta_{\rm shadow}(\varepsilon_{\rm p}) = B(\varepsilon_{\rm p})\left(\frac{R}{r_{\rm p}}\right)^{D(\varepsilon_{\rm p})}. \tag{A8}$$

For Saturn's case with $\varepsilon_{\rm p} = 26\overset{\circ}{.}7$, the best-fit values were found to be $B \simeq 0.5$ and $D \simeq -2.17$, indicating that the fraction of time a ring particle remains in eclipse decays approximately as the inverse square of the orbital distance from the planet, as shown in Figure 7. The result is also valid

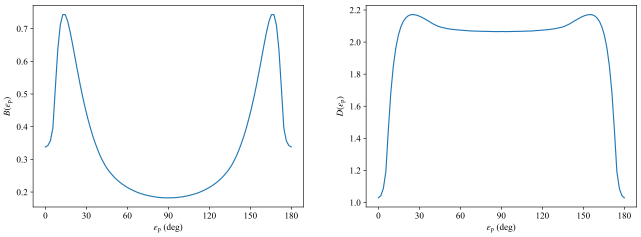

Figure 8. Values of $B(\varepsilon_{\rm p})$ and $D(\varepsilon_{\rm p})$ as a function of the planet obliquity $\varepsilon_{\rm p}$. The shadow fraction is $\eta_{\rm shadow}(\varepsilon_{\rm p}) = B(\varepsilon_{\rm p}) \times (R/r_{\rm p})^{D(\varepsilon_{\rm p})}$.

for the Martian system, whose obliquity is $25\overset{\circ}{.}2$. Figure 8 shows the values of $B(\varepsilon_{\rm p})$ and $D(\varepsilon_{\rm p})$ as a function of $\varepsilon_{\rm p}$ over the range $(0°, 180°)$.

Appendix B
Approximation for the EY Coefficient

As stated in Section 3.1, $f_{\rm EY}$ loses its dependence on the particle size when the size is larger than the characteristic thermal penetration r_0. When $r < r_0$, $f_{\rm EY}$ can be approximated as being proportional to r^3, as shown in Figure 9.

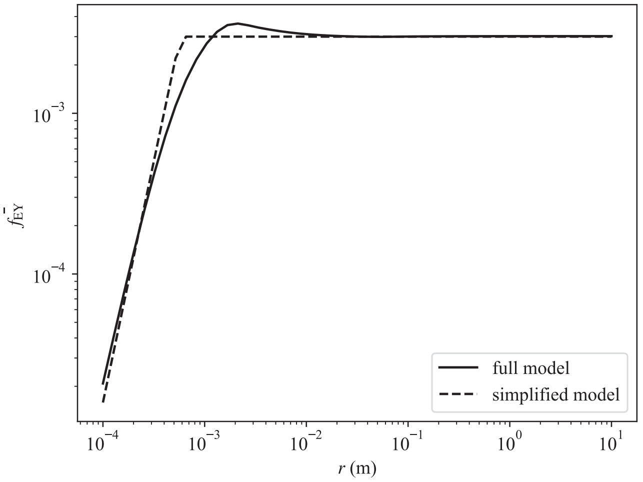

Figure 9. The dependence of the EY coefficient on the particle size. The full solution (Equations (11) and (12)) can be approximated as a piecewise function (Equation (17)) for easier integration.

Appendix C
The Formula for $\eta_{\rm Size}$ Considering a Power-law Size Distribution

The ring particles at an arbitrary layer with optical depth τ' can be assumed to follow a power law $dN = Cr^{-\alpha}dr$ with the minimum radius $r_{\rm min}$ and maximum radius $r_{\rm max}$. Constrained by the total mass, we obtain

$$C = \frac{3R\Delta R\Sigma(4-\alpha)}{2\rho(r_{\rm max}^{4-\alpha} - r_{\rm min}^{4-\alpha})}\frac{\Delta\tau'}{\tau} \tag{C1}$$

except for the singularity $\alpha = 4$ that leads to $C = 3R\Delta R\Delta\tau'\Sigma/2\rho\tau\ \ln(r_{\rm max}/r_{\rm min})$. The total torque of all particles in the annulus by the eclipse–Yarkovsky effect is

$$T_{\rm EY} = \int F_{\rm EY}RdN = \int_{r_{\rm min}}^{r_{\rm max}} F_{\rm EY}RCr^{-\alpha}dr. \tag{C2}$$

When $r_{\rm min} < r_0 < r_{\rm max}$, by substituting $F_{\rm EY}$, we obtained

$$\begin{aligned} T_{\rm EY} &= \frac{\pi(1-A_{\rm v})\,\Phi_{\rm s}f_{\rm EY,0}RC}{cr_0^3}e^{-\tau/\sin\psi}\frac{\Delta\tau'}{\tau} \\ &\quad\times\left(\int_{r_{\rm min}}^{r_0} r^{5-\alpha}dr + r_0^3\int_{r_0}^{r_{\rm max}} r^{2-\alpha}dr\right) \\ &= \frac{\pi(1-A_{\rm v})\,\Phi_{\rm s}f_{\rm EY,0}RC}{cr_0^3}e^{-\tau/\sin\psi}\frac{\Delta\tau'}{\tau} \\ &\quad\times\left(\frac{r_0^{6-\alpha} - r_{\rm min}^{6-\alpha}}{6-\alpha} + r_0^3\frac{r_0^{3-\alpha} - r_{\rm min}^{3-\alpha}}{3-\alpha}\right) \\ &= \frac{2\pi R^2\Delta R(1-A_{\rm v})\,\Phi_{\rm s}f_{\rm EY,0}}{c}\frac{\Delta\tau'}{\tau}\frac{3\Sigma}{4\rho r_0^3}\frac{4-\alpha}{r_{\rm max}^{4-\alpha} - r_{\rm min}^{4-\alpha}} \\ &\quad\times e^{-\tau/\sin\psi}\left(\frac{r_0^{6-\alpha} - r_{\rm min}^{6-\alpha}}{6-\alpha} + r_0^3\frac{r_0^{3-\alpha} - r_{\rm min}^{3-\alpha}}{3-\alpha}\right). \end{aligned} \tag{C3}$$

Considering the definition of the optical depth

$$\begin{aligned} \tau &= \frac{\sum\limits_i \pi r_i^2}{\sum m_i}\Sigma = \Sigma\frac{\displaystyle\int_{r_{\rm min}}^{r_{\rm max}} \pi r^2Cr^{-\alpha}{\rm d}r}{\displaystyle\int_{r_{\rm min}}^{r_{\rm max}} 4\pi\rho r^3Cr^{-\alpha}{\rm d}r/3} \\ &= \frac{3\Sigma}{4\rho}\frac{(4-\alpha)(r_{\rm max}^{3-\alpha} - r_{\rm min}^{3-\alpha})}{(3-\alpha)(r_{\rm max}^{4-\alpha} - r_{\rm min}^{4-\alpha})}, \end{aligned} \tag{C4}$$

where m_i is the mass of the ith particle, Equation (C3) becomes

$$\begin{aligned} T_{\rm EY} &= \frac{2\pi R^2\Delta R(1-A_{\rm v})\,\Phi_{\rm s}f_{\rm EY,0}}{c}\Delta\tau' e^{-\tau/\sin\psi} \\ &\quad\times\frac{3-\alpha}{r_{\rm max}^{3-\alpha} - r_{\rm min}^{3-\alpha}}\left(\frac{r_0^{6-\alpha} - r_{\rm min}^{6-\alpha}}{r_0^3(6-\alpha)} + \frac{r_{\rm max}^{3-\alpha} - r_0^{3-\alpha}}{3-\alpha}\right). \end{aligned} \tag{C5}$$

Comparing Equation (20) with Equation (C5), we obtain

$$\eta_{\rm size} = \frac{3-\alpha}{r_{\rm max}^{3-\alpha} - r_{\rm min}^{3-\alpha}}\left(\frac{r_0^{6-\alpha} - r_{\rm min}^{6-\alpha}}{r_0^3(6-\alpha)} + \frac{r_{\rm max}^{3-\alpha} - r_0^{3-\alpha}}{3-\alpha}\right). \tag{C6}$$

When $r_{\rm min} > r_0$, we have

$$T_{\rm EY} = \frac{\pi(1-A_{\rm v})\,\Phi_{\rm s}f_{\rm EY,0}RC}{c}e^{-\tau/\sin\psi}\frac{\Delta\tau'}{\tau}\left(\int_{r_{\rm min}}^{r_{\rm max}} r^{2-\alpha}{\rm d}r\right). \tag{C7}$$

Following the same procedure as above, we can obtain

$$\eta_{\rm size} = 1, \tag{C8}$$

which can also be deduced from Equation (C6) by discarding the first term in the bracket and replacing r_0 with $r_{\rm min}$ in the second term. The unity value of $\eta_{\rm size}$ is because $f_{\rm EY}$ has no dependence on the size r when $r > r_0$.

After calculating the case when $r_{\rm max} < r_0$, we obtain the complete form of $\eta_{\rm size}$:

$$\eta_{\rm size} = \begin{cases} 1, & r_{\rm max} > r_{\rm min} > r_0 \\ \dfrac{3-\alpha}{r_{\rm max}^{3-\alpha} - r_{\rm min}^{3-\alpha}}\left(\dfrac{r_0^{6-\alpha} - r_{\rm min}^{6-\alpha}}{r_0^3(6-\alpha)} + \dfrac{r_{\rm max}^{3-\alpha} - r_0^{3-\alpha}}{3-\alpha}\right), & r_{\rm max} > r_0 > r_{\rm min} \\ \dfrac{(3-\alpha)(r_{\rm max}^{6-\alpha} - r_{\rm min}^{6-\alpha})}{r_0^3(6-\alpha)(r_{\rm max}^{3-\alpha} - r_{\rm min}^{3-\alpha})}, & r_0 > r_{\rm max} > r_{\rm min} \end{cases} \tag{C9}$$

For Saturn's rings, observational studies suggest that the slope of the size–frequency distribution lies in the range $2.7 \lesssim \alpha \lesssim 3.2$ (K. E. Miller et al. 2024), which spans the singular point $\alpha = 3$ in $\eta_{\rm size}$ (the other singular point, $\alpha = 6$, is

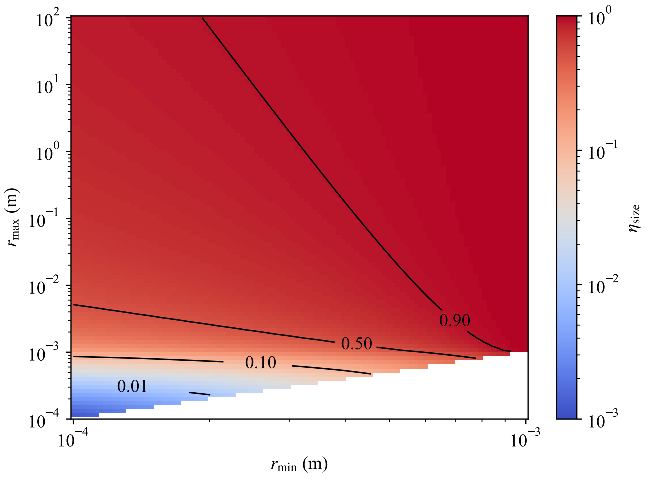

Figure 10. Size factor $\eta_{\rm size}$ as a function $r_{\min}$ and $r_{\max}$ for a power-law distribution with $\alpha = 3$. $r_{\min}$ is set to range to 1 mm since $\eta_{\rm size}$ equals 1 when $r_{\min} > 1$ mm.

unlikely to be realized). In addition, theoretical modeling predicts $\alpha \simeq 3$ (N. Brilliantov et al. 2015). We therefore adopt $\alpha = 3$ in this work. In the case of $\alpha = 3$, following the same procedure as described above, we have

$$\eta_{\rm size} = \begin{cases} 1, & r_{\max} > r_{\min} > r_0 \\ \dfrac{1}{\ln(r_{\max}\,/\,r_{\min})}\left(\dfrac{r_0^3 - r_{\min}^3}{3r_0^3} + \ln(r_{\max}/r_0)\right), & r_{\max} > r_0 > r_{\min} \\ \dfrac{r_{\max}^3 - r_{\min}^3}{3r_0^3\ln(r_{\max}\,/\,r_{\min})}, & r_0 > r_{\max} > r_{\min} \end{cases} \tag{C10}$$

The distribution of $\eta_{\rm size}$ is plotted as a function $r_{\min}$ and $r_{\max}$ in Figure 10.

As inferred from Equation (C9), when $\alpha < 3$, which corresponds to a shallow SFD, the term $(r_{\max}^{3-\alpha} - r_{\min}^{3-\alpha}) \sim r_{\max}^{3-\alpha}$ unless $r_{\max}$ and $r_{\min}$ are close. This indicates the largest particles will dominate $\eta_{\rm size}$. On the other hand, when $\alpha > 3$, the term $(r_{\max}^{3-\alpha} - r_{\min}^{3-\alpha}) \sim -r_{\min}^{3-\alpha}$. Therefore the smallest particles dominate $\eta_{\rm size}$ in this case. When $\alpha = 3$, both the largest and smallest particles affect $\eta_{\rm size}$ significantly, as inferred from Equation (C10).

Appendix D
Simulation Parameters in `Pkdgrav`

The parameters in the simulation generating Figure 4 are listed in Table 1.

ORCID iDs

Wen-Han Zhou https://orcid.org/0000-0003-4229-8936
Eiichiro Kokubo https://orcid.org/0000-0002-5486-7828
Harrison Agrusa https://orcid.org/0000-0002-3544-298X
Gregorio Ricerchi https://orcid.org/0009-0002-5271-8658
Aurélien Crida https://orcid.org/0000-0002-1293-9782
David Vokrouhlický https://orcid.org/0000-0002-6034-5452
Yun Zhang https://orcid.org/0000-0003-4045-9046
Ronald-Louis Ballouz https://orcid.org/0000-0002-1772-1934

References

Afonso, G., Barlier, F., Mignard, F., Carpino, M., & Farinella, P. 1989, AnGeo, 7, 501
Afonso, G., Gomes, R., & Florczak, M. 1995, P&SS, 43, 787
Ballouz, R.-L., Richardson, D. C., & Morishima, R. 2017, AJ, 153, 146
Blanc, M., Crida, A., Shibaike, Y., et al. 2025, SSRv, 221, 35
Bottke, W. F., Vokrouhlický, D., Rubincam, D. P., & Nesvorný, D. 2006, AREPS, 34, 157
Boudon, Y., Barlier, F., Bernard, A., et al. 1979, AcAau, 6, 1387
Braga-Ribas, F., Sicardy, B., Ortiz, J. L., et al. 2014, Natur, 508, 72
Brilliantov, N., Krapivsky, P., Bodrova, A., et al. 2015, PNAS, 112, 9536
Burns, J. A., Lamy, P. L., & Soter, S. 1979, Icar, 40, 1
Canup, R., & Salmon, J. 2018, SciA, 4, eaar6887
Chesley, S. R., Ostro, S. J., Vokrouhlický, D., et al. 2003, Sci, 302, 1739
Ciarniello, M., Filacchione, G., Nicholson, P. D., et al. 2024, SSRv, 220, 72
Citron, R. I., Genda, H., & Ida, S. 2015, Icar, 252, 334
Craddock, R. A. 2011, Icar, 211, 1150
Crida, A., & Charnoz, S. 2012, Sci, 338, 1196
Crida, A., Estrada, P. R., Nicholson, P. D., & Murray, C. D. 2025, SSRv, 221, 66
Ćuk, M., & Burns, J. A. 2005, Icar, 176, 418
Ćuk, M., El Moutamid, M., Lari, G., et al. 2024, SSRv, 220, 20
Cuzzi, J., Clark, R., Filacchione, G., et al. 2009, in Saturn from Cassini-Huygens, ed. M. K. Dougherty, L. W. Esposito, & S. M. Krimigis (Springer), 459
Cuzzi, J. N., & Durisen, R. H. 1990, Icar, 84, 467
Durisen, R. H. 1984, in Planetary Rings, ed. R. Greenberg & A. Brahic (Univ. of Arizona Press), 416
Durisen, R. H., Cramer, N. L., Murphy, B. W., et al. 1989, Icar, 80, 136
Esposito, L. 2014, Planetary Rings (Cambridge Univ. Press)
Estrada, P. R., & Durisen, R. H. 2023, Icar, 400, 115296
Farinella, P., Nobili, A., Barlier, F., & Mignard, F. 1990, A&A, 234, 546
Farinella, P., & Vokrouhlický, D. 1996, P&SS, 44, 1551
Farinella, P., Vokrouhlický, D., & Hartmann, W. K. 1998, Icar, 132, 378
Fenucci, M., Micheli, M., Gianotto, F., et al. 2024, A&A, 682, A29
French, R. G., McGhee-French, C. A., Lonergan, K., et al. 2017, Icar, 290, 14
Fuller, J. 2014, Icar, 242, 283
Goldreich, P., & Tremaine, S. 1978a, Icar, 34, 227
Goldreich, P., & Tremaine, S. 1978b, Icar, 34, 240
Hamilton, D. P., & Krivov, A. V. 1996, Icar, 123, 503
Hamilton, D. P., & Ward, W. R. 2004, AJ, 128, 2510
Hedman, M. M., Burns, J. A., Evans, M. W., Tiscareno, M. S., & Porco, C. C. 2011, Sci, 332, 708
Hedman, M. M., Burns, J. A., Hamilton, D. P., & Showalter, M. R. 2013, Icar, 223, 252
Hedman, M. M., Burns, J. A., Showalter, M. R., et al. 2007, Icar, 188, 89
Hesselbrock, A. J., & Minton, D. A. 2017, NatGe, 10, 266
Hyodo, R., & Ida, S. 2025, ApJ, 994, 15
Ip, W.-H. 1984, Icar, 60, 547
Kambara, Y., & Kokubo, E. 2025, ApJ, 985, 71
Lebedew, P. 1910, ApJ, 31, 385
Liu, X., Hou, X.-Y., Yang, Z.-T., Gan, Q.-B., & Zhang, Y. 2023, ApJ, 950, 50
Loudon, R., & Baxter, C. 2012, RSPSA, 468, 1825
Madeira, G., Charnoz, S., Zhang, Y., et al. 2023, AJ, 165, 161
Miller, K. E., Filacchione, G., Cuzzi, J. N., et al. 2024, SSRv, 220, 70
Morgado, B. E., Sicardy, B., Braga-Ribas, F., et al. 2023, Natur, 614, 239
Morishima, R., & Salo, H. 2004, Icar, 167, 330
Morishima, R., Spilker, L., Salo, H., et al. 2010, Icar, 210, 330
Ohtsuki, K. 2005, ApJL, 626, L61
Ohtsuki, K. 2006a, Icar, 183, 373
Ohtsuki, K. 2006b, Icar, 183, 384
Öpik, E. J. 1951, PRIA, 54A, 165
Perrine, R. P., & Richardson, D. C. 2012, Icar, 219, 515
Perrine, R. P., Richardson, D. C., & Scheeres, D. J. 2011, Icar, 212, 719
Porco, C., Baker, E., Barbara, J., et al. 2005, Sci, 307, 1226
Poynting, J. H. 1904, RSPTA, 202, 525
Richardson, D. C., Quinn, T., Stadel, J., & Lake, G. 2000, Icar, 143, 45
Robertson, H. P. 1937, MNRAS, 97, 423
Rosenblatt, P., Charnoz, S., Dunseath, K. M., et al. 2016, NatGe, 9, 581
Rubincam, D. P. 1982, CeMec, 26, 361
Rubincam, D. P. 1987, JGR, 92, 1287
Rubincam, D. P. 1988, JGR, 93, 13805
Rubincam, D. P. 1990, JGRB, 95, 4881
Rubincam, D. P. 1995, JGRE, 100, 1585
Rubincam, D. P. 2006, Icar, 184, 532
Rubincam, D. P. 2013, Icar, 226, 1618
Rubincam, D. P. 2014, Icar, 239, 96
Saillenfest, M., Lari, G., & Boué, G. 2021, NatAs, 5, 345
Salmon, J., Charnoz, S., Crida, A., & Brahic, A. 2010, Icar, 209, 771
Salo, H. 1995, Icar, 117, 287
Scheirich, P., Pravec, P., Jacobson, S. A., et al. 2015, Icar, 245, 56
Scheirich, P., Pravec, P., Kušnirák, P., et al. 2021, Icar, 360, 114321

Scheirich, P., Pravec, P., Meyer, A. J., et al. 2024, PSJ, 5, 17

Schwartz, S. R., Richardson, D. C., & Michel, P. 2012, Granular Matter, 14, 363

Singer, S. F. 1967, in The Seventh International Space Science Symposium, 317, ed. A. Dollfus

Slabinski, V. J. 1997, CeMDA, 66, 131

Spilker, L. J., Ferrari, C., Altobelli, N., Pilorz, S., & Morishima, R. 2018, in Planetary Ring Systems. Properties, Structure, and Evolution, ed. M. S. Tiscareno & C. D. Murray (Cambridge Univ. Press), 399

Stadel, J. G. 2001, PhD thesis, University of Washington

Strom, R. G., Croft, S. K., & Barlow, N. G. 1992, in Mars, ed. H. H. Kieffer, B. M. Jakosky, C. W. Snyder, & M. S. Matthews (Univ. of Arizona Press), 383

Tajeddine, R., Nicholson, P. D., Longaretti, P.-Y., El Moutamid, M., & Burns, J. A. 2017, ApJS, 232, 28

Tiscareno, M. S., & Harris, B. E. 2018, Icar, 312, 157

Tiscareno, M. S., & Murray, C. D. 2018, Planetary Ring Systems: Properties, Structure, and Evolution (Cambridge Univ. Press)

Torii, N., Ida, S., Kokubo, E., & Michikoshi, S. 2025, Icar, 439, 116608

Vokrouhlický, D. 1999, A&A, 344, 362

Vokrouhlický, D., Bottke, W. F., Chesley, S. R., Scheeres, D. J., & Statler, T. S. 2015, in Asteroids IV, ed. P. Michel, F. E. DeMeo, & W. F. Bottke (Univ. of Arizona Press), 509

Vokrouhlický, D., Nesvorný, D., Chesley, S. R., & Ostro, S. J. 2005, Icar, 179, 128

Vokrouhlický, D., Nesvorný, D., Dones, L., & Bottke, W. F. 2007, A&A, 471, 717

Ward, W. R. 1973, Sci, 181, 260

Ward, W. R., & Hamilton, D. P. 2004, AJ, 128, 2501

Wyatt, S. P., & Whipple, F. L. 1950, ApJ, 111, 134

Zhang, Y., & Lin, D. N. 2020, NatAs, 4, 852

Zhang, Y., Michel, P., Barnouin, O. S., et al. 2022, NatCo, 13, 4589

Zhang, Y., Richardson, D. C., Barnouin, O. S., et al. 2017, Icar, 294, 98

Zhou, W.-H. 2024, A&A, 692, L2

Zhou, W.-H., Vokrouhlicky, D., Kanamaru, M., et al. 2024, ApJL, 968, L3